EFFECTS OF LAYERING, DIPPING ANGLE, AND FAULTING ON TWO-DIMENSIONAL, VARIABLY SATURATED FLOW

Iterative Performance Assessment- Phase II

Prepared for

Nuclear Regulatory Commission
Contract NRC-02-88-005

Prepared by

Center for Nuclear Waste Regulatory Analyses
San Antonio, Texas

February 1992

CNWRA 92-004

EFFECTS OF LAYERING, DIPPING ANGLE, AND FAULTING ON TWO-DIMENSIONAL VARIABLY SATURATED FLOW

Iterative Performance Assessment - Phase II

Prepared for

Nuclear Regulatory Commission
Contract NRC-02-88-005

Prepared by

Amvrossios C. Bagtzoglou, Rachid Ababou, and Budhi Sagar

Center for Nuclear Waste Regulatory Analyses
San Antonio, Texas

February 1992

TABLE OF CONTENTS

LIST OF FIGURES

LIST OF FIGURES (Continued)

LIST OF FIGURES (Continued)

LIST OF TABLES

EXECUTIVE SUMMARY

This report documents results of unsaturated flow simulations undertaken as an auxiliary analysis for the Iterative Performance Assessment (IPA) Phase 2 Project. The primary objective of the simulations is to study the effect on flow of common geological features, such as nonhorizontal stratification and vertical or near-vertical fault zones intersecting the strata, in a two-dimensional or "thin slice" domain.

The simulations begin with the assumption of homogeneity; features such as layers, dip angle, and fault zone are added later to study their effect on the flow field. The problems inherent in specifying initial and boundary conditions that are consistent with infiltration rates and hydrologic properties are discussed. In the simulations presented here, a method of developing consistent initial and boundary conditions for more complex problems is adopted that depends upon steady state solution of simpler problems. The most complex geometry assumes five layers of equal thickness with a dip angle of 6 degrees to the East, a fault zone intersecting the strata orthogonally, and infiltration of 50 mm/year. The emphasis in these simulations is on process modeling rather than predictive modeling. Even though there is some similarity between the stratigraphy of the adopted problem and that of Yucca Mountain, there are other major differences between the two. For that reason, results presented here are not representative of the Yucca Mountain flow conditions.

The results indicate that the presence of layers and crosscutting fault zones tend to induce three-dimensional unstable flows in the unsaturated zone. The instability is manifested in our simulations by an oscillatory behavior of steady-state. That is, at large times, the solution fluctuates and does not tend to converge to a single value. We also observe that specification of initial and boundary conditions for unsaturated flow simulations is problematic. Inappropriate initial and boundary conditions can cause significant errors in the final results.

This was only a preliminary study. We propose that in IPA Phase III, a fully three-dimensional study be undertaken that will include, as far as possible, the known properties of the Yucca Mountain site. The effect of assumptions made in specifying initial and boundary conditions, and in constraining the system to be of lower dimensionality, would then be studied in such three-dimensional simulations.

1 INTRODUCTION

To fulfill its mandate of licensing a High-Level Nuclear Waste Repository under the Nuclear Waste Policy Act, as amended (1982 and 1987), the U.S. Nuclear Regulatory Commission (NRC) is developing methods and procedures for an efficient and effective review of Department of Energy's (DOE's) license application. The Center for Nuclear Waste Regulatory Analyses (CNWRA or Center) at Southwest Research Institute (SwRI) is a Federally Funded Research and Development Center created to assist the NRC in this endeavor.

Iterative Performance Assessment (IPA) is one of the approaches adopted by the NRC and Center staffs to develop their methods and capabilities with respect to license application review. In addition, the IPA work is expected to be useful for the NRC-DOE interactions during the pre-licensing period. The work reported in this document was performed as a part of Phase 2 of the IPA effort.

IPA Phase 2 includes performance assessment of the total waste isolation system and detailed auxiliary analysis of selected important features of subsystems. Assessing performance of a geologic repository requires execution of a number of steps. These include conceptualizing the system in terms of its identifiable components, the formulation of mathematical models representing all important processes, the translation of mathematical models into computer programs, the verification and to the extent possible validation of the models, the analyzing of laboratory and field data to extract model parameters, the executing of computer programs, performing sensitivity and uncertainty analyses, and, finally, analyzing results to draw conclusions. During each iteration of the IPA, an effort is made to execute as many of these steps as possible.

The main objective of the auxiliary analyses in IPA is to provide support to simplifications made in performance assessment of the total system by obtaining better understanding of a subsystem through detailed analysis. Detailed analyses of flow in fully and partially saturated domains containing heterogeneous porous media and discrete fractures were planned as auxiliary analyses in the IPA Phase 2. Analyses of saturated flow in a region containing Yucca Mountain were reported earlier (Ahola and Sagar, 1992). Ahola and Sagar (1992) reported fluctuations of water table for various cases including hypothesized changes in recharge/discharge conditions and modifications in stratigraphy. In this report, analysis of the flow field in variably saturated zone is developed to understand the effect of stratigraphic layering, presence of a fault zone and the dipping of layers. The analysis is performed for a deep (approximately 530 meters) hard rock system. Some of the data for the analysis were taken from the Yucca Mountain project reports but it was freely modified to enhance the effects that are being studied.

Specifically, this is not an analysis of flow in the unsaturated zone at Yucca Mountain. Hydraulic and stratigraphic parameters only resemble the Yucca Mountain site. For example, the depths to water table, the number of geologic strata, their dipping angle, and the existence of a fault zone are characteristics that are preserved in the present analysis. The width of the fault zone, the exact net infiltration rate, and the exact hydraulic parameters of the matrix and fault media

are **not** honored. Therefore, conclusions regarding suitability of Yucca Mountain for the proposed nuclear waste repository are not directly derivable from this analysis. Rather, the objective of this analysis is to help develop assumptions that may be useful in formulating the flow module for the total system performance assessment.

Many aspects of flow in the partially saturated zone are worthy of detailed study; for a comprehensive review of partially saturated flow, see Ababou (1991a). This effort is limited to two-dimensional flow simulations in a porous medium consisting of several layers whose bedding plane may or may not be orthogonal to the gravity vector and which are intersected by a fault zone. The simulations were performed in a transient mode to study the manner in which the solutions to the flow equation approach steady-state.

The report is organized as follows. In Section 2, the numerical model embodied in the BIGFLO computer code and used for the analysis is discussed. The data employed in conceptualizing the problem, and preliminary tests, are described in Section 3. Variations in data used in subsequent simulations are also described in that section. Simulation results in the presence of layers, fault, and dip, are presented in Section 4. Finally, Section 5 contains a summary of the report along with conclusions.

2 NUMERICAL CODE DESCRIPTION

Numerical modeling of subsurface flow systems requires efficient discretization, solution, and data processing methods, particularly when dealing with fully three-dimensional heterogeneous material properties and initial-boundary conditions. In this section, we describe the numerical strategy employed in the BIGFLO code (Ababou, 1988), and develop some analyses of computational requirements, and numerical tests of large three-dimensional simulations in saturated and unsaturated, imperfectly stratified, heterogeneous earth materials.

The BIGFLO software package was initially developed at the Massachusetts Institute of Technology for investigating three-dimensional flow in random porous media [Ababou, 1988]. The package comprises two modular Fortran 77 codes: a data processor called FLOPROC and a simulation code called BIGFLO. The package is undergoing modifications, in order to enhance its scope, flexibility, and computational efficiency. Full documentation of the upgraded package will be developed at a later stage.

The BIGFLO simulation code accommodates three-dimensional transient or steady flow in saturated, partially saturated, or purely unsaturated porous media with heterogeneous or spatially random hydrodynamic coefficients. The porous medium is assumed to satisfy a local mass conservation equation (of the form $\partial\theta/\partial t = -\nabla \cdot q$) and the Darcy-Buckingham constitutive law (of the form $q = -K\nabla H$). The governing equation is expressed in terms of total hydraulic head for saturated flow, and in terms of moisture content and pressure head for partially saturated and unsaturated flow. In the latter case, a mixed variable formulation of Richards' equation is used. That is:

$$\frac{\partial\theta(h,\mathbf{x})}{\partial t} = \nabla\left[K(h,x)(\nabla h + \mathbf{g})\right], \qquad (2\text{-}1)$$

where $H = h + \mathbf{g} \cdot \mathbf{x}$ is the total hydraulic head potential (m), h is pressure head (m), θ is volumetric water content (m^3/m^3), K is hydraulic conductivity (m/s), and $\mathbf{g}$ is the cosine vector aligned with, and opposed to, the acceleration of gravity and equal to (0, 0, +1) if the third axis is vertical and pointing upwards.

The differential equations are discretized by an implicit finite difference scheme, two-point backward Euler in time, and seven-point centered in space. The spatial mesh is a regular rectangular lattice. The time step is generally variable and self-adjusted. The computational domain is a three-dimensional parallelepiped, whose coordinate system may be inclined at arbitrary angles with respect to the natural, horizontal-vertical coordinate system.

Multi-dimensional inputs to the simulation code are specified either node-by-node or block-by-block with the aid of the interactive data processor, FLOPROC. The multi-dimensional input functions are the initial conditions, the planar boundary conditions, and up to six three-dimensional parameters for spatially variable hydrodynamic coefficients and nonlinear constitutive relations. The boundary conditions are of three types: (i) pressure or hydraulic head,

(ii) normal flux, or (iii) zero pressure gradient for "gravitational drainage". Spatially variable and mixed-type boundary conditions can be defined separately for each of the six boundary planes. Irregular boundaries can be introduced, in some cases, by selecting extremely small or large conductivity values in subregions located between the physical flow domain and the outer computational boundaries. Low-dimensional flow systems are simulated by reducing the size of the grid to just a few nodes, i.e. at least one interior node plus two boundary nodes, along any unmodeled dimension. Low-dimensional datasets such as transects and cross-sections can be either generated by the simulation code, or extracted from existing three-dimensional datasets by the data processing code.

The interactive data processor serves as a convenient tool for certain pre-processing tasks such as setting up boundary conditions and material properties, and for post-processing tasks such as cell-by-cell calculation of three-dimensional flux vectors, spatial-statistical analyses, extraction of sub-dimensional datasets, and so on. Auxiliary graphic techniques for displaying large three-dimensional datasets have also been developed (Ababou, 1991a, Chap.6).

The flow simulator solves nonlinear equations in the case of unsaturated or partially saturated flow, and linear equations in the special case of fully saturated flow. In the latter case, a sparse symmetric matrix system is generated at each time step. Steady flow problems can be solved either directly, based on steady-state equations equivalent to one infinite time step, or indirectly, by time-stepping the transient flow equations up to very large times. For nonlinear flow problems, a modified Picard iteration scheme is used. This yields a sequence of sparse symmetric matrix systems converging to the solution of the nonlinear system at each time step (outer iterations). The linearized systems have the same seven-diagonal structure as in the linear case.

The solutions of the symmetric matrix systems are obtained by a fast preconditioned iterative solver (inner iterations). Several *sparse* solution modules that qualify as "fast preconditioned iterative solvers" are presently available, including the Strongly Implicit Procedure (SIP) and Diagonal Scaling Conjugate Gradients (DSCG). All arrays are stored in-core, and a diagonal-by-diagonal matrix storage scheme is used. This data structure minimizes in-core memory requirements and CPU time. Furthermore, the code dynamically allocates the correct dimensions to the various arrays that describe the flow system. For a given set of inputs, the simulation code computes the total size of the master array needed for storage of all vector-matrix variables, and starts the simulation only if the declared size is sufficient.

The total in-core memory required to simulate fully heterogeneous three-dimensional systems is modest, about 10 words per node for saturated flow, and roughly twice as much for partially saturated or unsaturated flow. Thus, owing to the efficiency and sparseness of discretization and solution procedures, relatively large simulations are feasible in reasonable amounts of computer time and with minimal memory requirements. In the case of saturated flow, grid size can be on the order of two hundred thousand nodes for a minicomputer such as Microvax-2, and typically one to ten million nodes for the 1985-90 generation of supercomputers such as Cray-2. For partially saturated flow problems, the "feasible" grid size can decrease by up to one order of

magnitude relative to the linear case, depending on the nature of nonlinearities and initial-boundary conditions.

In the case of *unsaturated* flow in highly heterogeneous media, our experience so far indicates that the best strategy for steady-state solution is to implement a time-marching method, i.e. by simulating transient flow up to very large times using the dynamic time-stepping capability of the BIGFLO code [Ababou, 1988]. In the transient mode, the space-time discretization requirements for unsaturated flow simulations are essentially of two types: (i) constraints due to inherently nonlinear and advective-like terms in the mixed form of Richards' equation, and (ii) constraints due to the spatial heterogeneity of unsaturated conductivity and saturation curves.

Several patterns of material heterogeneity have been previously tested with the BIGFLO package, including the case of two-dimensional unsaturated multi-layered media, and the case of three-dimensional anisotropic (imperfectly stratified) random media. Examples of applications of the code for saturated as well as unsaturated heterogeneous flow systems can be found in Ababou (1991b). The BIGFLO code was also used by others to analyze patterns of flow and contaminant transport in real or synthetic three-dimensional formations with various types of heterogeneities (e.g. Tompson and Gelhar 1990; Townley and Trefry 1990; Townley et al., 1991). In what follows, some of the simulated flow systems will include a sub-vertical fault. The fault will be modeled as a special thin vertical layer of very coarse material having highly contrasted properties relative to the surrounding porous matrix.

3 PROBLEM CONCEPTUALIZATION

3.1 FLOW SYSTEM AND COMPUTATIONAL DOMAIN

The hydrogeologic properties in the unsaturated zone of Yucca Mountain, Nevada, were taken into account in order to reproduce to a small extent the general features of the site in our simulations. However, since this preliminary investigation was oriented towards analysis of processes rather than predictive modeling, no attempt was made at using all the available hydrogeologic properties of the site in our example problem.

Yucca Mountain consists of a series of North-trending fault-block ridges composed of layers of volcanic ash tuffs that generally have a regional dip of 5 to 7 degrees to the East (Scott and Bonk, 1984). The proposed repository area, depicted in Figure 3-1, is also bounded by steeply dipping faults or by fault zones, and is transected by a few normal faults. Therefore, it is important to study the effects of layering, regional dipping, and fault zones on unsaturated water flow. For more details on what is known about the hydrogeology of Yucca Mountain, the reader is referred to DOE's Site Characterization Plan. It is also summarized in a report by Ababou (1991a).

In the simulations presented herein, the computational domain was assumed to consist of five layers having hydrogeologic properties shown in Table 3-1. The five layers are assumed to have approximately equal thicknesses spanning a total depth of 530m at which depth the water table is assumed to be located. The geometric mean and standard deviation of the hydrologic properties of the Calico Hills nonvitrified (CHnv) member of Yucca Mountain provide the basis for assigning properties to the five layers in this model. This is explained in Section 3.2 below.

The computational domain used in these simulations is based on a three-dimensional cartesian grid system. The axes of this system are aligned with East-West (X-axis), North-South (Y-axis), and vertical (Z-axis). The dimensions of the computational domain are 615 m, 80 m, and 530 m in the X-, Y-, and Z-directions, respectively. For the preliminary simulations discussed in this section, the domain is discretized into $29 \times 5 \times 54$ nodes comprising of a total of 7,830 nodes (Figure 3-2). For simulations described in Section 4, the domain size is doubled in the X-direction by doubling the grid size along this direction.

Initial-boundary conditions are taken uniform in the Y-axis. In principle, taking no-flux conditions on the North-South boundaries (orthogonal to the Y-axis) should make the flow system effectively two-dimensional in (X,Z), with no flow in the Y-direction. As will be seen, however, this may or may not be the case if pressure conditions are used instead (see discussion of results later in this section).

3.2 HYDRAULIC PARAMETERS USED IN THE STUDY

Several functional forms of pressure-dependent hydraulic conductivity, K(h), and pressure-dependent water content, θ(h), have been proposed in the literature, some based on

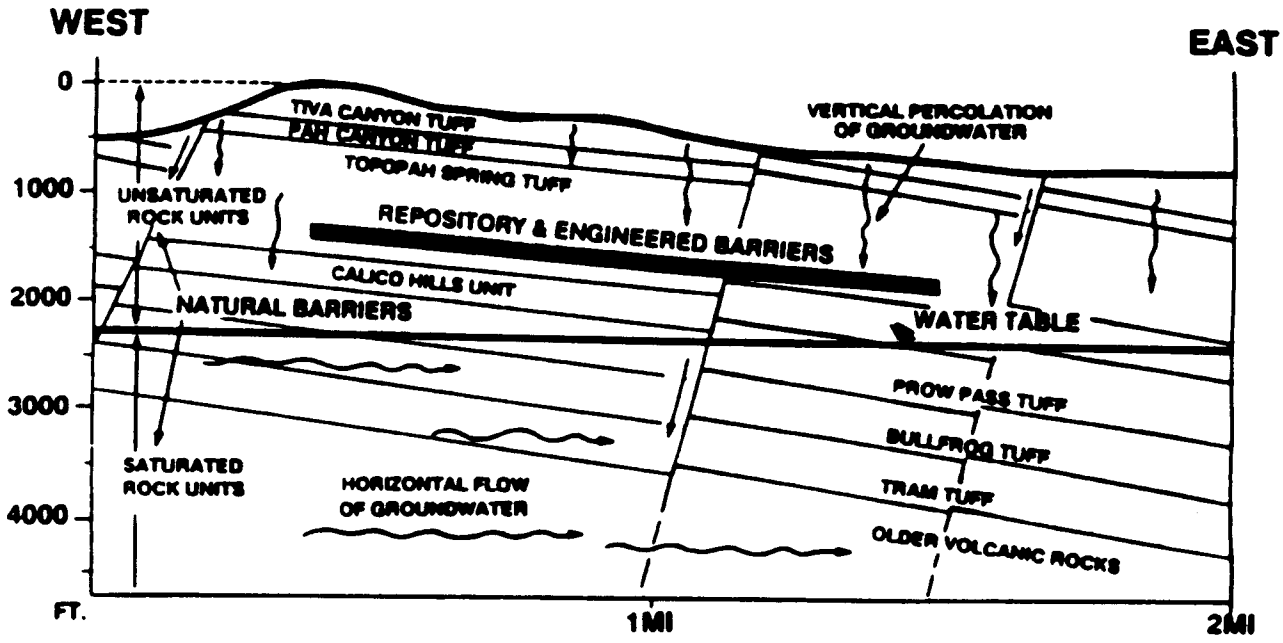

Figure 3-1. East-West cross-section through Yucca Mountain showing the volcanic stratigraphy, the potential repository site, the unsaturated zone, and the water table (Mattson et al., 1992)

semi-empirical models of unsaturated flow through idealized porous media. The functional forms used herein are the exponential Gardner model for K(h) and the van Genuchten model for θ(h). The choice of these particular models is for convenience and other models may be more appropriate for the site.

The exponential conductivity model reads:

$$K(h) = K_s \exp[\alpha(h - h_b)] \quad \text{if } h \leq h_b$$

$$K(h) = K_s \quad \text{if } h > h_b \,, \tag{3-1}$$

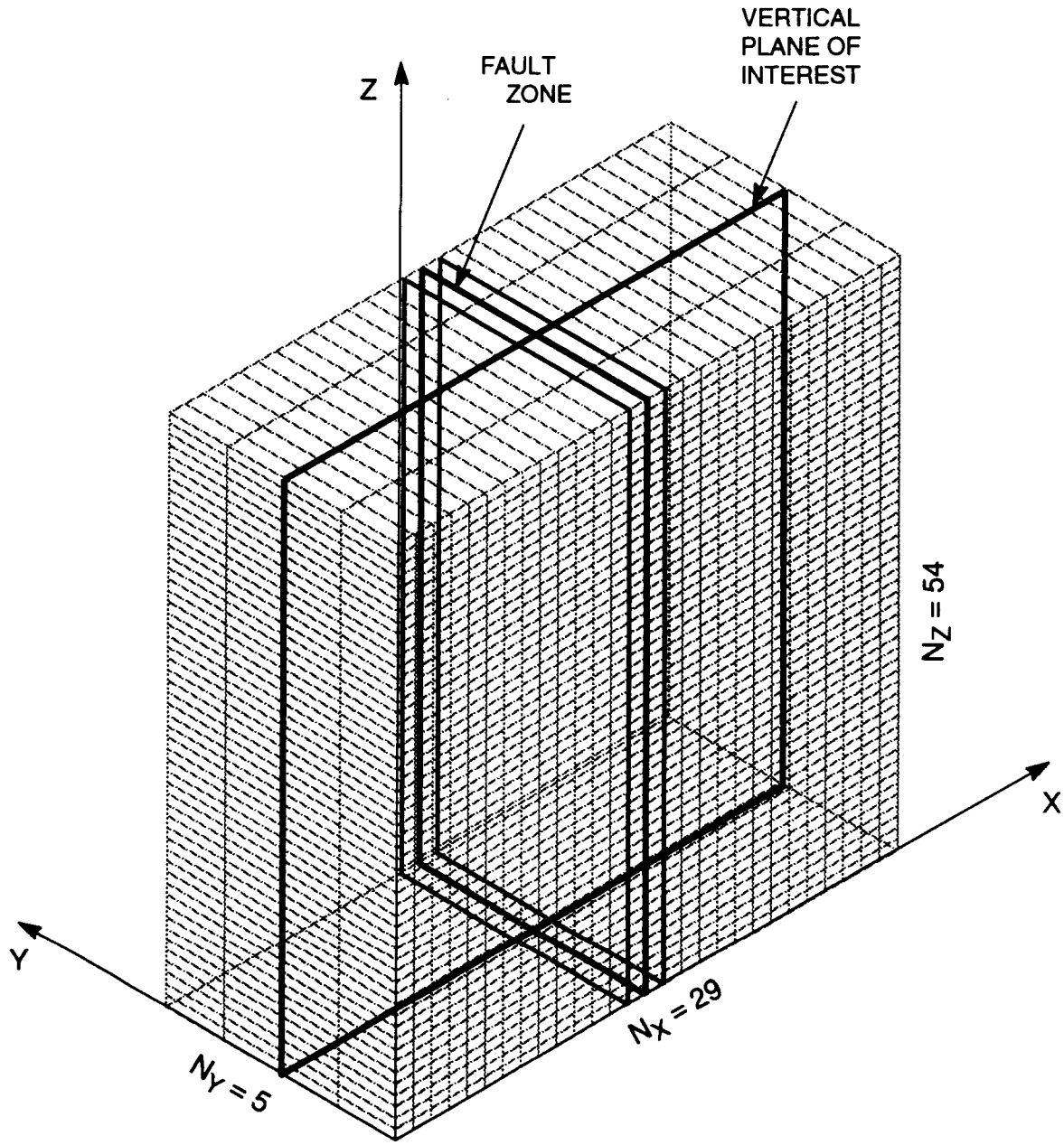

Figure 3-2. Schematic representation of computational grid showing the fault zone. The plane y = 40 m, where all results are plotted, is shown in bold.

where K_s is the saturated hydraulic conductivity, α is a characteristic inverse length scale or capillary diffusivity (Ababou 1991a), h is the pressure, and h_b is the air-entry pressure.

The van Genuchten model for the retention curve is:

$$\theta(h) = \theta_r + (\theta_s - \theta_r) [1 + (-\beta h)^n]^{-m} , \qquad (3\text{-}2)$$

where θ_s and θ_r are the saturated and residual water moisture contents, respectively, β is a characteristic inverse length, and n and m are real exponents. These exponents are related by the Mualem constraint:

$$m = 1 - \frac{1}{n} , \qquad (3\text{-}3)$$

where $0 < m < 1$, and $n > 1$. Conceptually, the inverse parameter β^{-1} is analogous to an air entry pressure for the water retention curve. This observation suggests that h_b and β^{-1} should be approximately equal, or at least on the same order of magnitude.

The saturated conductivity (K_s) and slope parameters (m and n) are, generally, spatially varying functions in all three dimensions. In the present work, however, they are assumed to be constant within a layer. The layer properties are, further, assumed to be log-deviations around the geometric mean of each respective parameter, taken herein as representative of the Calico Hills unit. Accordingly, for a typical hydraulic parameter ω, we have for the five layers:

$$\omega_1 = \omega_3 = \omega_5 = \omega_G \exp(+\sigma_{\ln\omega}) \qquad (3\text{-}4a)$$

$$\omega_2 = \omega_4 = \omega_G \exp(-\sigma_{\ln\omega}) . \qquad (3\text{-}4b)$$

The parameter ω_G is the geometric mean of ω_1 and ω_2, and $\sigma_{\ln\omega}$ represents the standard deviation of the log-property computed from its spatial variation in a representative matrix which was chosen to be the CHnv unit at Yucca Mountain. The general relation given in (3-4) applies to the parameters K_s, α, h_b and β. The remaining matrix parameters are assumed to be constant in all layers, and are assigned typical values of the CHnv unit. Thus, $\theta_s = 44.11\%$, $\theta_r = 1.89\%$, $n = 3.872$, and $m = 0.7417$.

The fault was arbitrarily modeled as a three-cell wide, YZ-planar zone located in the middle of the domain, with air-entry pressure head approximately half the corresponding value for the rock matrix. The saturated hydraulic conductivity of the fault is assumed 40 times greater than the undisturbed matrix saturated hydraulic conductivity. Both ratios pertain to the geometric means of the respective parameters. Table 3-1 summarizes the hydraulic properties discussed above for the matrix layers and fault zone.

Table 3-1. VALUES OF SPATIALLY VARIABLE HYDRAULIC PARAMETERS

Parameters	K_S (m/d)	α (m^{-1})	h_b (m)	β (m^{-1})
Geo.Mean ω_G	2.33×10^{-2}	2.2×10^{-2}	20	5×10^{-2}
Std.Dev. $\sigma_{ln\omega}$	1.0	0.2	0.2	0.2
Coarse Layers (1, 3, and 5)	6.334×10^{-2}	2.687×10^{-2}	16.375	6.1×10^{-2}
Fine Layers (2 and 4)	8.572×10^{-3}	1.801×10^{-2}	24.428	4.09×10^{-2}
Fault Zone	9.32×10^{-1}	1.0×10^{-1}	10.417	9.6×10^{-2}

The values of these parameters, when substituted in Equation 3-1, yield three different types of pressure-dependent curves K(h) as shown in Figure 3-3. It is worthwhile noticing that the fault hydraulic conductivity is much greater than the geometric average matrix hydraulic conductivity near saturation, and remains higher for values of suction head up to about 50 m. On the other hand, the fault becomes less conductive than the matrix for values of suction head significantly higher than 50 m (suction is the opposite of pressure, that is $\psi = -h$). The existence of a crossing point, where the fault becomes less permeable than the matrix, is of particular interest and, as will be shown later in this work, affects directly the overall behavior of the flow system.

To further quantify the above observations, a plot of the variation of hydraulic conductivity with depth is depicted in Figure 3-4. This plot is based on an assumed initial water moisture content distribution corresponding to a net infiltration rate of 50 mm/year. This initial moisture profile will be developed and used in the simulations to be presented in the next section. The plot emphasizes the fact that the crossing point, discussed above, translates to a moisture profile-dependent depth where the fault and matrix flow properties become reversed. For the assumed moisture profile, the crossing point is located within the layer adjacent to the water table and at a depth of approximately 50-60 m above the water table. However, the depth of the crossing point is highly dependent on flow conditions, whether they originate from assumed, computed, or observed initial and boundary conditions.

The regional dip is assumed to be 6 degrees to the East (Rockhold et al., 1989 unpublished report). This dip results in an approximate 10 percent fraction of the body (gravity) force being parallel to the X-axis attached to the dipped domain. Note that the dip is introduced

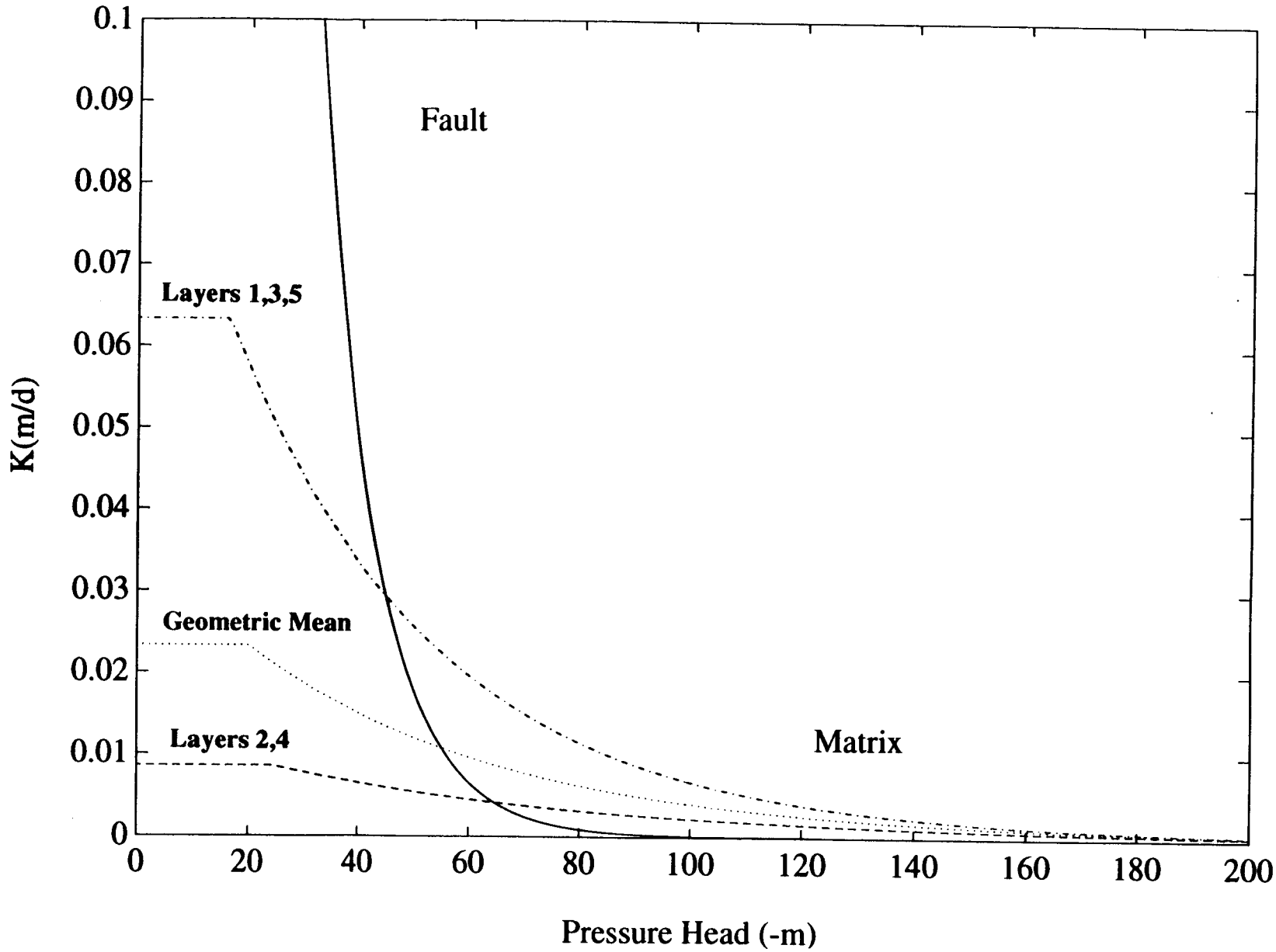

Figure 3-3. Matrix and fault exponential hydraulic conductivity models. Solid line: fault, dotted line: Matrix geometric mean, dashed and dashed-dotted lines: Matrix layers 2 and 4, and 1, 3, and 5, respectively.

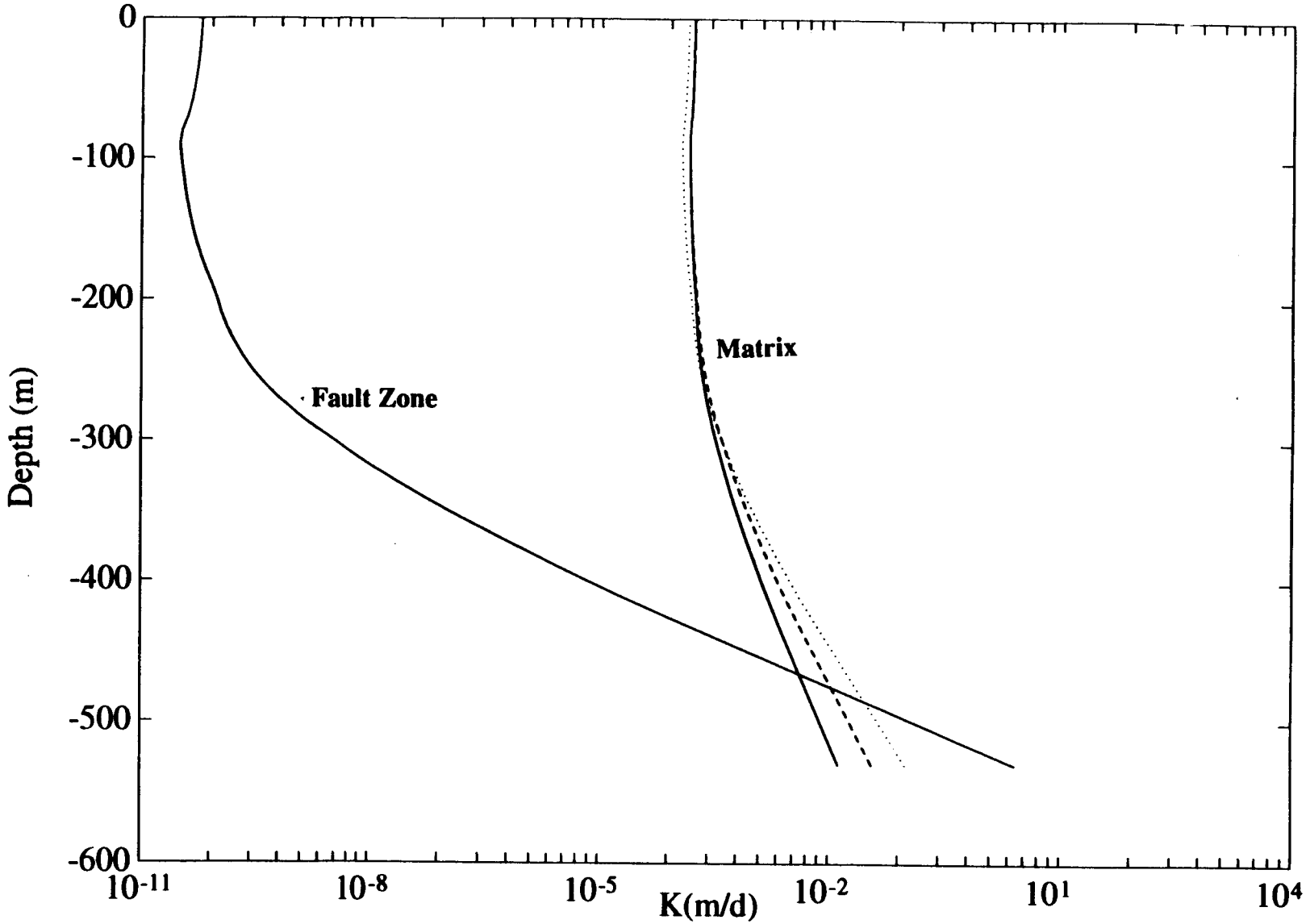

Figure 3-4. Variation of hydraulic conductivity with depth for an arbitrary spatial distribution of water moisture. The three matrix curves correspond to the individual coarse and fine layers and their geometric mean.

by changing the orientation of the gravity vector with respect to the domain. Therefore, the entire rectangular domain is dipped without any distortion of the relative arrangement of layers and fault. The layers become sub-horizontal and the fault becomes sub-vertical, at a 6 degree angle with respect to the horizontal and vertical axes, respectively.

Finally, the net infiltration rate q_o at the ground surface is taken to vary from 0 to 50 mm/year. In particular, the low value $q_0 = 0$ will be used as a minimal base case (e.g. initially hydrostatic conditions), while the high value $q_0 = 50$ mm/year will account for the potential occurrence of extreme infiltration conditions.

3.3 PRELIMINARY SIMULATIONS WITH HOMOGENEOUS PROPERTIES, NON-HYDROSTATIC INITIAL-BOUNDARY CONDITIONS, AND 1 MM/YEAR INFILTRATION RATE

This section presents a preliminary set of simulations which helped identify problems related, in particular, to the choice of initial-boundary conditions. We used here a "wet" non-hydrostatic pressure profile for both initial and boundary conditions:

$$h = -\frac{194}{530} Z \,, \qquad (3\text{-}5)$$

where Z is upwards and such that $Z = 0$ at the water table, $Z = 530$ m at ground surface. This pressure profile approximates linearly the piecewise initial and boundary conditions given in Sagar and Runchal (1990), who in turn deduced their initial conditions from saturation values given by Montazer and Wilson (1984). All lateral boundary conditions were taken to be fixed pressure head, based on Eqn. (3-5), except for the left (West) boundary which was assumed to be impervious. The right (East) boundary represents a fault zone in this particular simulation.

The above approach will be later revised to include a fault zone inside the computational domain, for reasons which will appear more clearly below. Recall that, in the present simulation, the fault is represented by a fixed pressure boundary, based on a pressure profile thought to be representative of average conditions.

The hydrodynamic properties used in these preliminary simulations were as follows. We used, for the entire domain, homogeneous unsaturated properties corresponding to the Calico Hills Non-Vitrified (CHnv) unit adapted from Sagar and Runchal (1990). However, the unsaturated conductivity curve K(h) was assumed to be exponential, with an assumed value of $\alpha = d(\ln K)/dh$ chosen to match approximately the Mualem-van Genuchten K(h) curve used in that report. It should be noted that the CHnv unit has much larger K_s than the other units, e.g. about two to three orders of magnitude higher than the overlying Topopah Spring Welded Unit (TSw) where the potential repository would be located.

The simulation results obtained for a net infiltration rate $q_0 = 1$ mm/year are depicted in Figures 3-5 through 3-7. Figure 3-5 depicts the time-evolution of global mass balance during

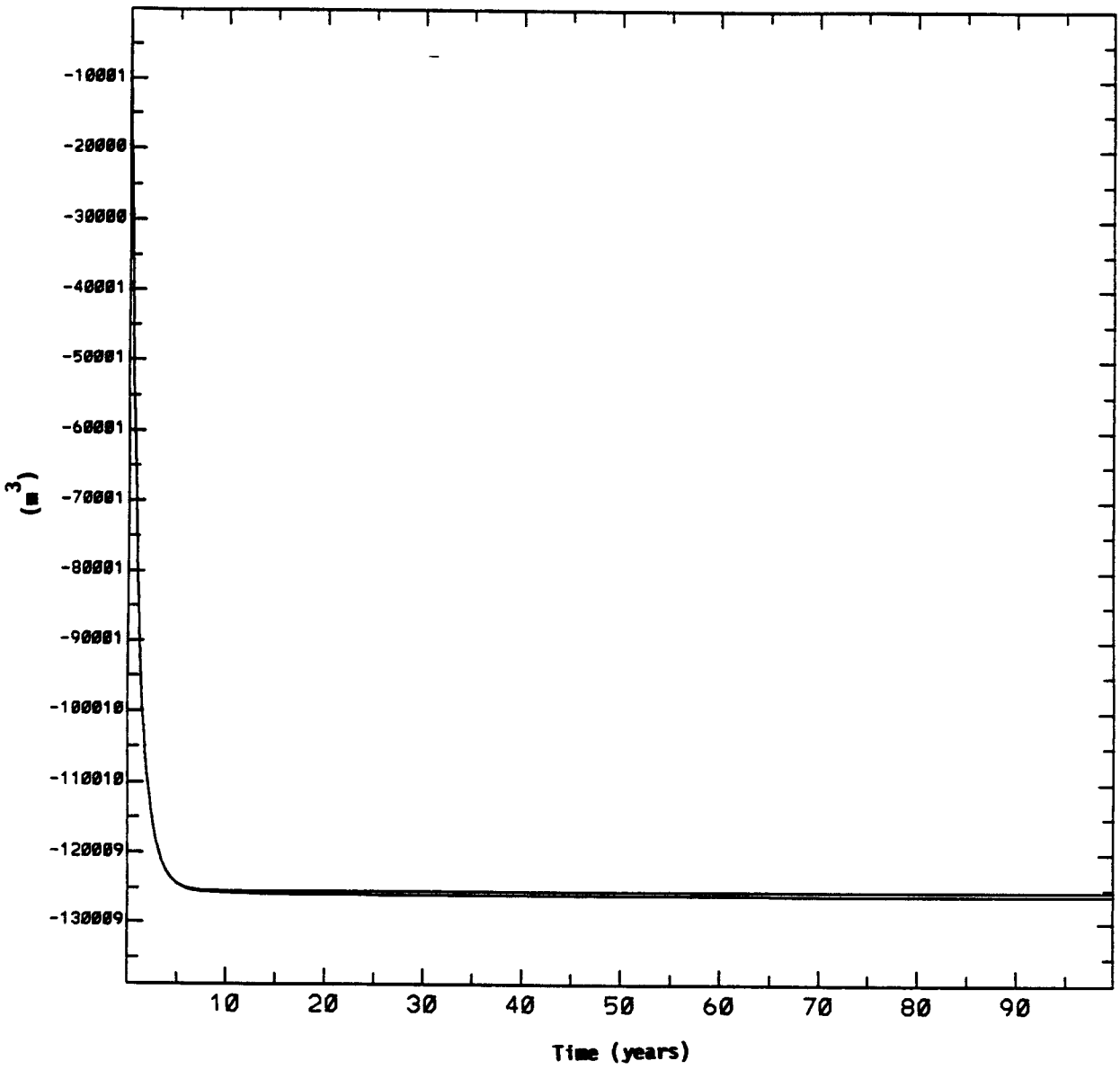

Figure 3-5. Time variation of total mass in the system for problem of Section 3.3: VMASS(t) is spatially integrated water content, and VBOUND(t) is time-cumulated net discharge rate through boundaries

100 years. The net increase of total mass of water in the domain was computed in two different ways, first by accumulating (in time) the net discharge rates through all boundaries (VBOUND or V_B for short), and secondly, by integrating (in space) the volumetric water contents (VMASS or V_M for short). The curves $V_B(t)$ and $V_M(t)$ are almost indistinguishable, which indicates excellent mass balance over the 100-year simulation. Either curve can be used to analyze the approximate transient behavior of the system. Thus, Figure 3-5 indicates that a steady-state (except for some possible redistribution of moisture within the domain) was reached after 5-10 years, the total mass in the system remaining constant thereafter. This was also confirmed from detailed pressure head distributions.

Figures 3-6 and 3-7 depict the quasi-steady pressure contours obtained at time $t \approx 5$ years, in a horizontal X-Y cross-section (Figure 3-6) and in a vertical X-Z cross-section (Figure 3-7). Note that these figures are not to scale, that is, the cross-sections appear to be square instead of rectangular; this is an artifact of the plotting package used for these particular figures. The pressure contours demonstrate that the flow system is not two- but three-dimensional. They also indicate that a significant quantity of water is continuously entering through the North, South, and also to a lesser degree, through the East boundary where the fault zone is located. Due to these lateral flows, the downward percolation rate through the water table (bottom boundary) is larger than the imposed net rainfall rate of 1 mm/year. The arrows sketched on Figures 3-6 and 3-7 indicate roughly the orientation and magnitude of flow through each boundary, based on inspection of other numerical outputs not shown here.

Finally, note that the steady-state pressure distribution is significantly "dryer" than the assumed initial condition. This is also supported by the mass balance Figure 3-5, which shows a large net loss of mass (or volume) of water, approximately 400 mm/year from time zero to steady-state. This means that, in addition to (or despite) lateral inflows, the water initially present in the system has been partially drained. It must be concluded that the assumed initial conditions do not reflect ambient (steady-state) conditions, and/or the assumed net infiltration rate of 1 mm/year does not reflect the in-situ (steady-state) rate, and/or the assumed properties do not reflect (even on average) the in-situ properties. However, the reader needs to note that the properties used here do not represent Yucca Mountain's unsaturated zone.

3.4 APPROACH TO CONSISTENT INITIAL AND BOUNDARY CONDITIONS

It may be useful at this point to recall the main objectives of this study. The objectives are to simulate and investigate the steady-state flow system in a two-dimensional (thin slice) vertical cross-section taking into account three main features:

(1) Bedding, represented by five layers;

(2) Presence of one subvertical fault; and

(3) Regional dip of the bedded units, approximately six degrees to the East.

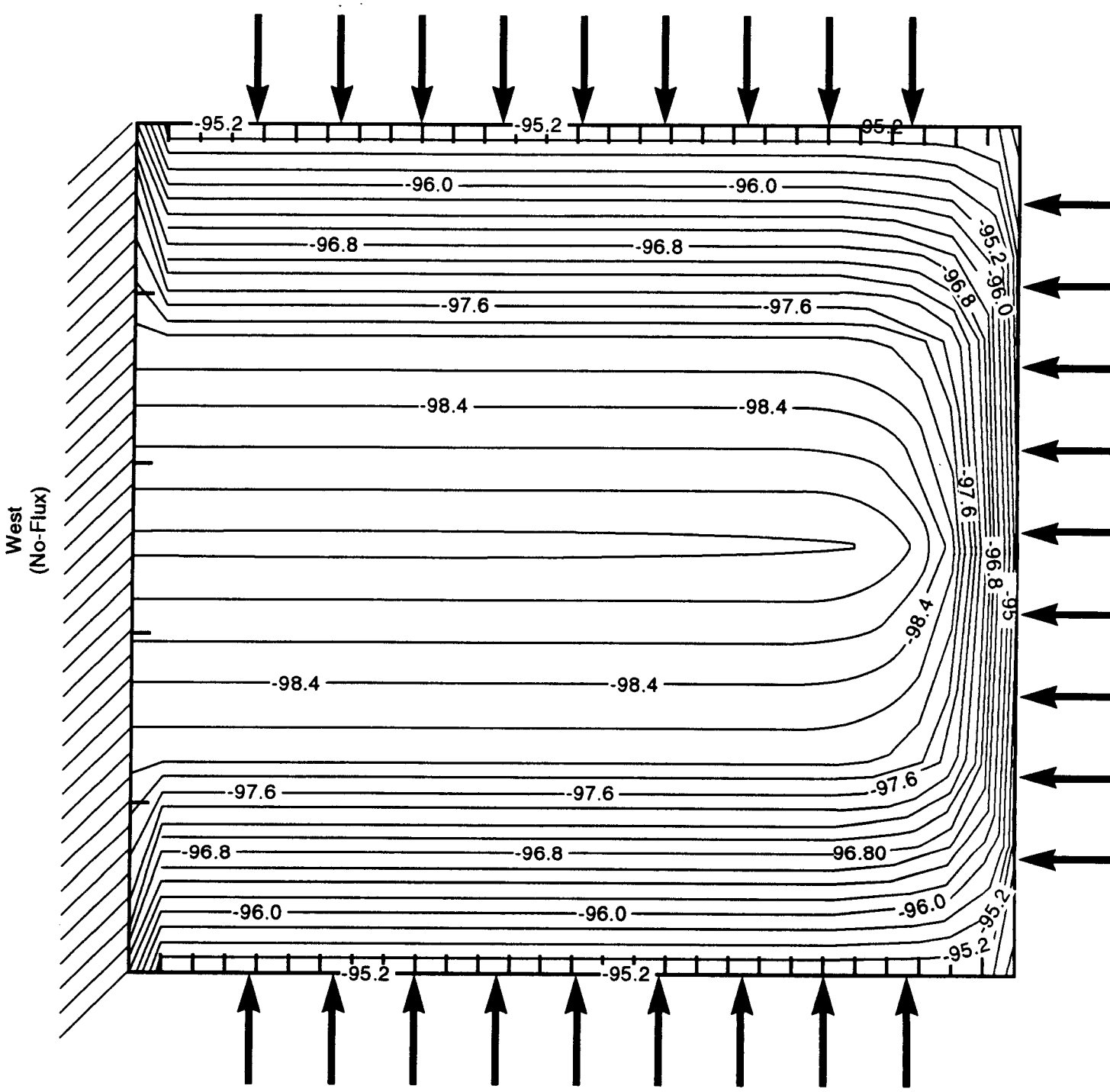

Figure 3-6. Contour plot of pressure head for t = 10 years for case involving homogeneous properties. Horizontal plane at Z = 265 m.

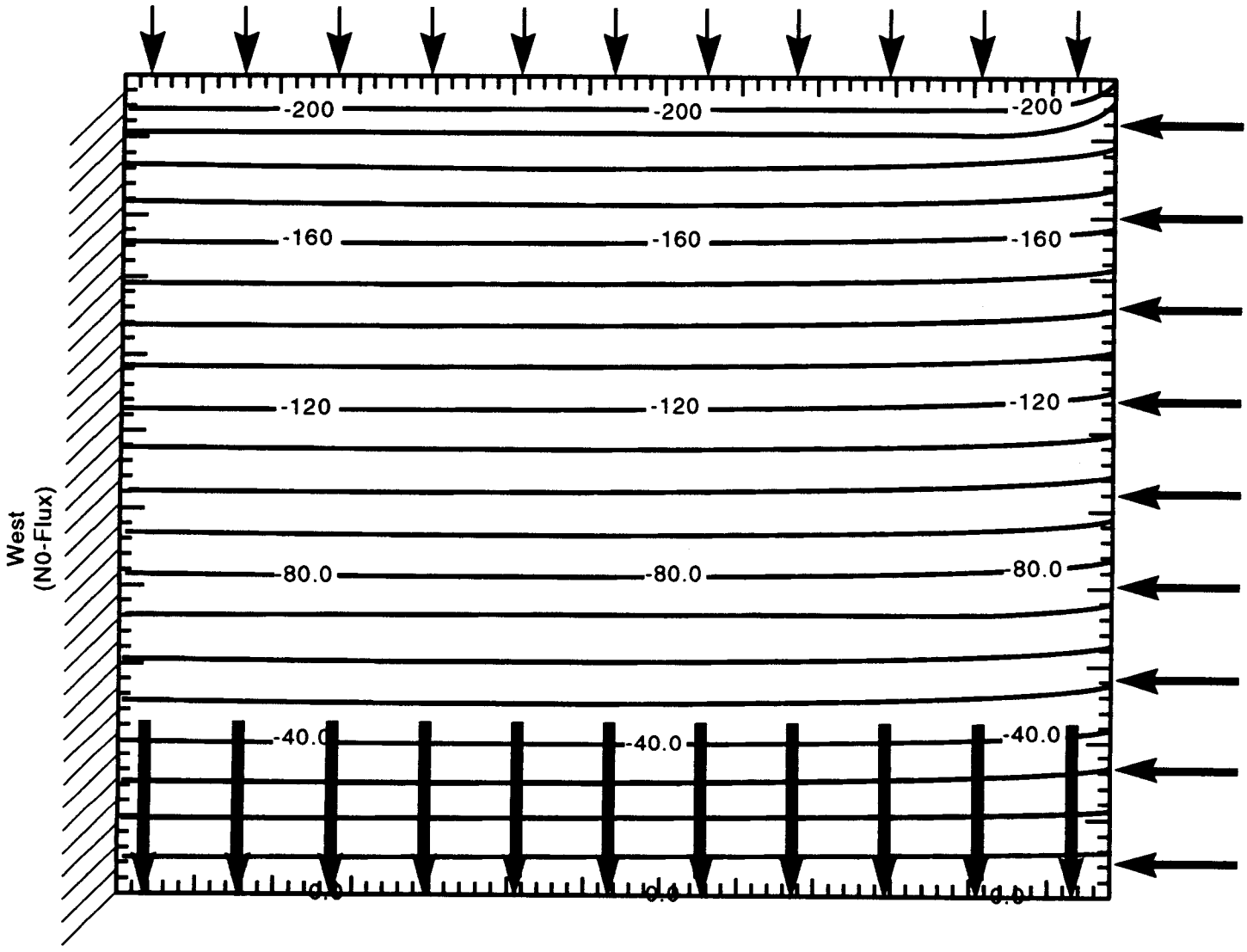

Figure 3-7. Contour plot of pressure head for t = 10 years for case involving homogenous properties. Vertical plane at Y = 40 m.

In addition, we are interested in exploring the behavior of the system for a range of net infiltration rates, up to relatively large values (50 mm/year).

Given the observations made in the previous section, it appears important to devise a method for generating initial-boundary conditions that are consistent with (i) the assumed input infiltration rate, and (ii) the assumed material properties of the strata. Our premise is that neither of these data are generally known with sufficient accuracy from available in-situ measurements. In what follows, we will include the fault in the interior of the computational domain rather than have it as a boundary. This will avoid making any "a priori" guess on the flow conditions within the fault plane, although there will still be a boundary condition imposed on the North-South boundaries which the fault intersects (indeed, the fault zone must touch both boundaries, since the North and South boundaries are artificially close to each other in this "thin slice" simulation). Furthermore, we will use the steady-state solutions of auxiliary or intermediate problems, in order to generate consistent initial and boundary conditions for the flow problem of interest.

In the case at hand, some artificial boundary conditions are needed for the East-West and for the North-South lateral boundaries. This is due in part to the fact that the cross-section is represented as a rectangular domain bounded above by an assumed regular surface and bounded below by the water table, rather than a more complicated domain following the actual Yucca Mountain topography. In addition, even if the actual topography were used, artificial lateral boundaries connecting ground surface to water table would still be needed, particularly for the East-West faces. The main problem is that there are no simple, natural conditions that can be used for these artificial boundaries.

To be sure, the number of "active" lateral boundaries can be reduced by assuming no-flux conditions on some of them. Thus, imposing no-flux conditions on the North-South boundaries would force the flow system to be strictly two-dimensional (in a vertical plane). However, imposing no-flux on the East-West boundaries as well, seems to be an overly restrictive and artificial constraint. For screening purposes, our approach will be to avoid any use of the "no-flux" assumption. The flow systems that result can be either two-dimensional, or "mildly" three-dimensional, given that the computational domain is a thin slice comprising only a few nodes along the North-South direction.

Appendix A gives a justification and motivation of the need for "consistent" boundary conditions. A simple example is developed in this appendix to show how the use of partially incorrect or lacunary field data can lead to inconsistent results. Briefly, our approach to generate more consistent initial-boundary conditions is one of successive approximation. We first solve an unsaturated flow problem to infinite time (steady-state) for a given net infiltration rate (q_o) but in the absence of a fault zone or dip in the stratigraphy, using no-flux conditions on all lateral boundaries. We then introduce a fault in the middle of the domain, and/or a regional dip angle $\theta = 6$ degrees to the East. A new simulation is conducted for this flow problem, using now the pressure head solutions of the previous problem as initial-boundary conditions. The same net infiltration rate q_o is applied on the top boundary.

Figure 3-8 gives a schematic description of the proposed approach to consistent initial-boundary conditions. This succession of simulations will now be applied to several infiltration rates, including:

(1) *"Dry" case*: $q_o = 0$ mm/year.

(2) *"Wet" case*: $q_o = 50$ mm/year.

There are other alternative ways of designing successive approximations for obtaining consistent initial-boundary conditions. Some of these are depicted in Figure 3-9. Our present choice is highlighted by bold arrows. Given the large number of choices available, the forthcoming numerical investigation will be conducted by using somewhat simpler stratigraphy and material properties than those used in Sagar and Runchal (1990). Nevertheless, unlike the previous simulations of Section 3.3, the key features mentioned earlier are explicitly represented, namely: bedding, dip, and fault. Results are analyzed in the next chapter.

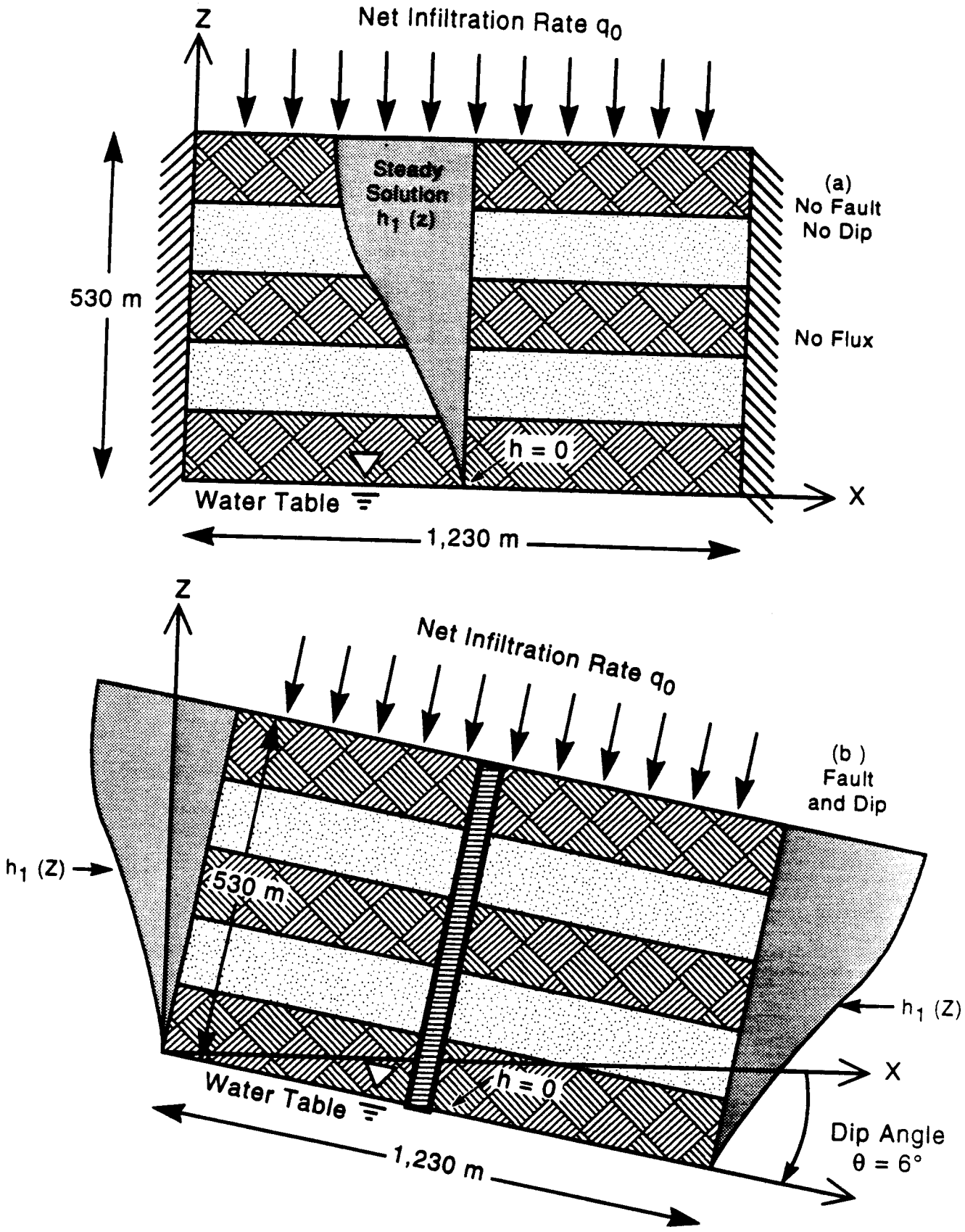

Figure 3-8. Schematic description of successive approximation approach to address the issue of consistent initial and boundary conditions

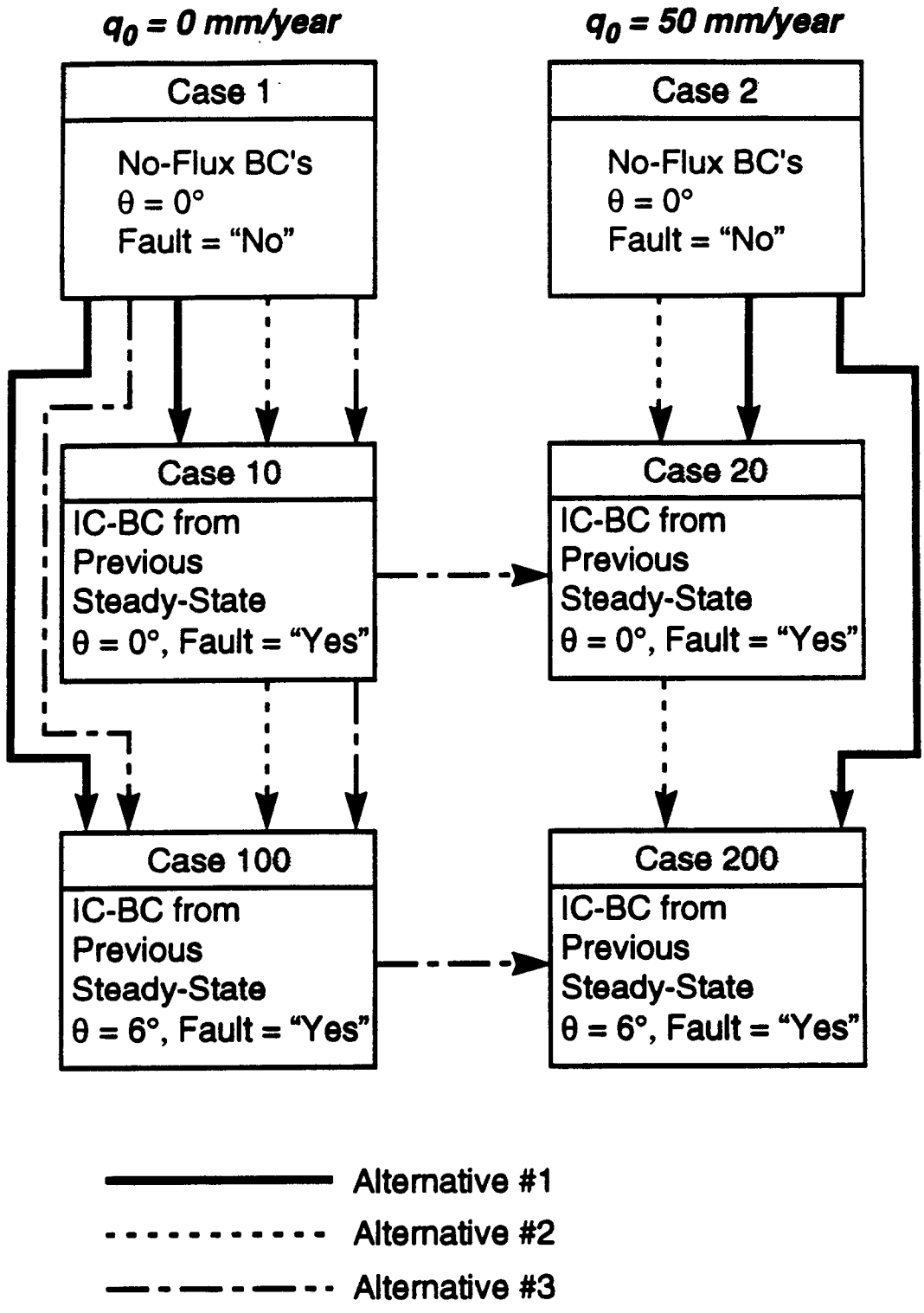

Figure 3-9. Flowchart conceptualization of proposed approach to address the issue of consistent initial and boundary conditions

4 SIMULATION RESULTS AND DISCUSSION

4.1 FLOW FIELD IN THE ABSENCE OF FAULT ZONE AND DIP (CASES 1 AND 2 OF FIGURE 3-9)

The flow system with five layers was, at first, simulated for a total period of 500 years, using no-flux conditions on all lateral boundaries. This length of time was found to be necessary for steady-state flow conditions to be achieved. In addition to the two hydroclimatic cases, corresponding to q_o = 0 and 50 mm/year, one extra set of simulations corresponding to q_o = 1 mm/year is also undertaken. The initial condition, assumed in all these simulations, is the linear pressure head profile of Equation (3-5).

Figure 4-1 depicts the temporal variation of the vertical pressure head profile, at the central transect Y=40 m, X = 615 m, under a net infiltration rate of q_o = 0 mm/year. Similar plots are shown in Figures 4-2 and 4-3 for infiltration rates q_o = 1 and 50 mm/year, respectively. It can be seen that for the q_o = 0 mm/year, steady-state is obtained only after 500 years of simulation. It is also apparent that the steady-state solution is much "drier" than the assumed initial condition of Eqn.(3-5), emphasizing the need for consistency of initial boundary conditions discussed in the previous section. It can be observed, further, that the effect of stratification in hydraulic properties is felt only during the early times of the simulation. The steady-state solution is a linear hydrostatic pressure head profile, not influenced by stratigraphy, as expected on theoretical grounds.

Results for the q_o = 1 mm/year case are similar, with two notable exceptions. First, steady-state is achieved faster (250 years). Secondly, due to the continuous influx of water from the top boundary, a non-hydrostatic pressure head profile is attained, as expected. The infiltration affects only the pressure profile in the coarse top layer (down to a depth of 100 m). Finally, for the extremely wet case (q_o = 50 mm/year), the behavior of the flow system changes drastically. Note, that case 2 uses the results of case 1 (q_o = 0 mm/year) as initial conditions. It should also be kept in mind that lateral boundary conditions were zero-flux throughout the simulation. It can be clearly seen that steady-state flow conditions are attained even faster, that is, after only 100 years of simulation. It is also worthwhile noticing that the effect of layering on pressure distribution appears to be almost insignificant for this flow rate, although the influence of the coarse top layer is still perceptible.

For this last simulation, mass balance and steady-state convergence criteria are presented in Figures 4-4 and 4-5. In the case of transient flow, total mass conservation implies that the net discharge rate through boundaries, $Q_B(t)$, should equal the rate of change of total mass in the flow domain, $Q_M(t)$. It is obvious from Figure 4-4 that there is good agreement between Q_M and Q_B for the course of all 500 years of simulation. Moreover, since both discharge rates reach net values very close to zero after about 100 years, it is concluded that steady-state conditions are achieved at this time. Similar observations can be made by plotting the measure

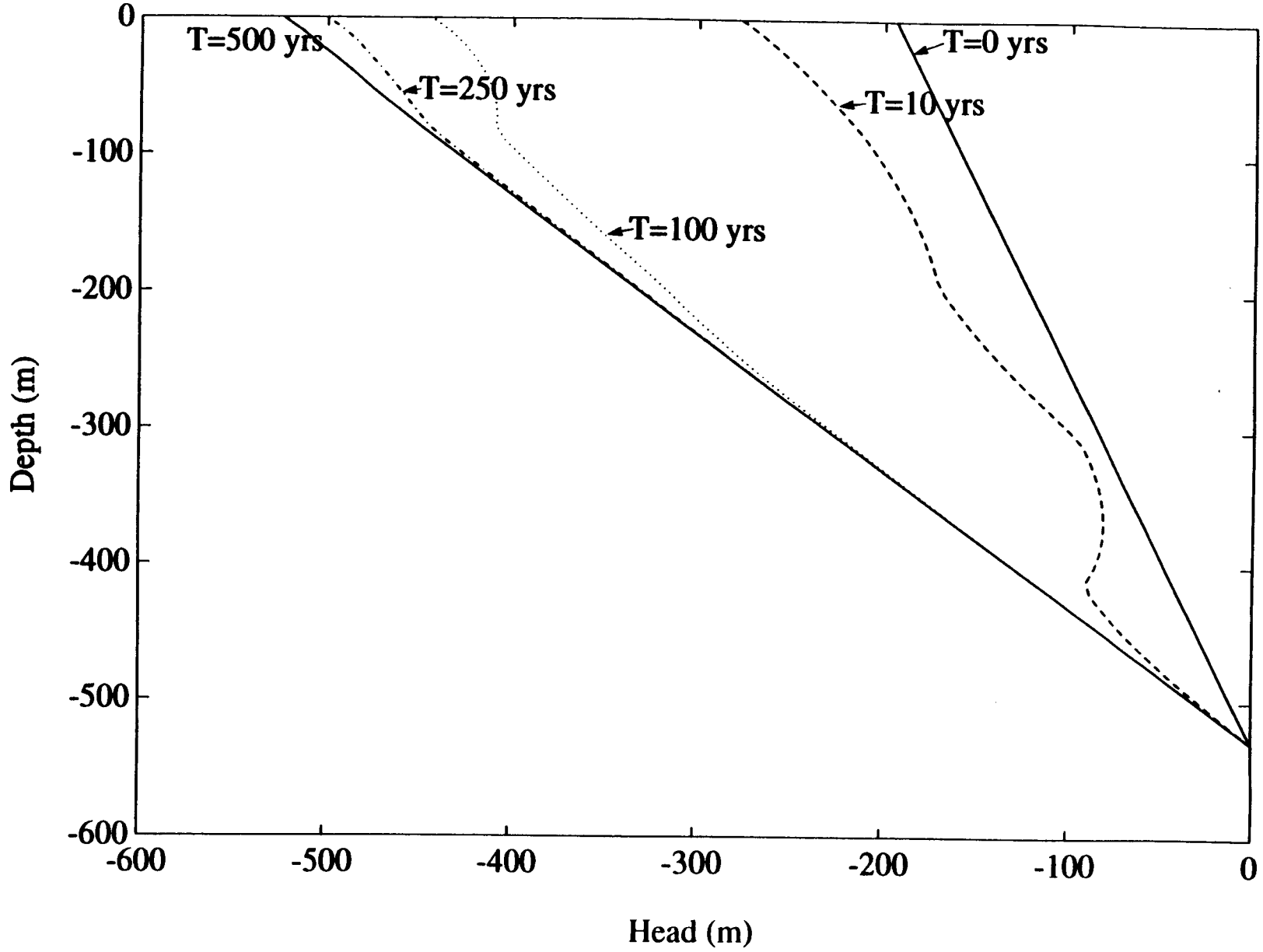

Figure 4-1. Temporal variation of pressure head profile for case 1 with q_o = 0 mm/year

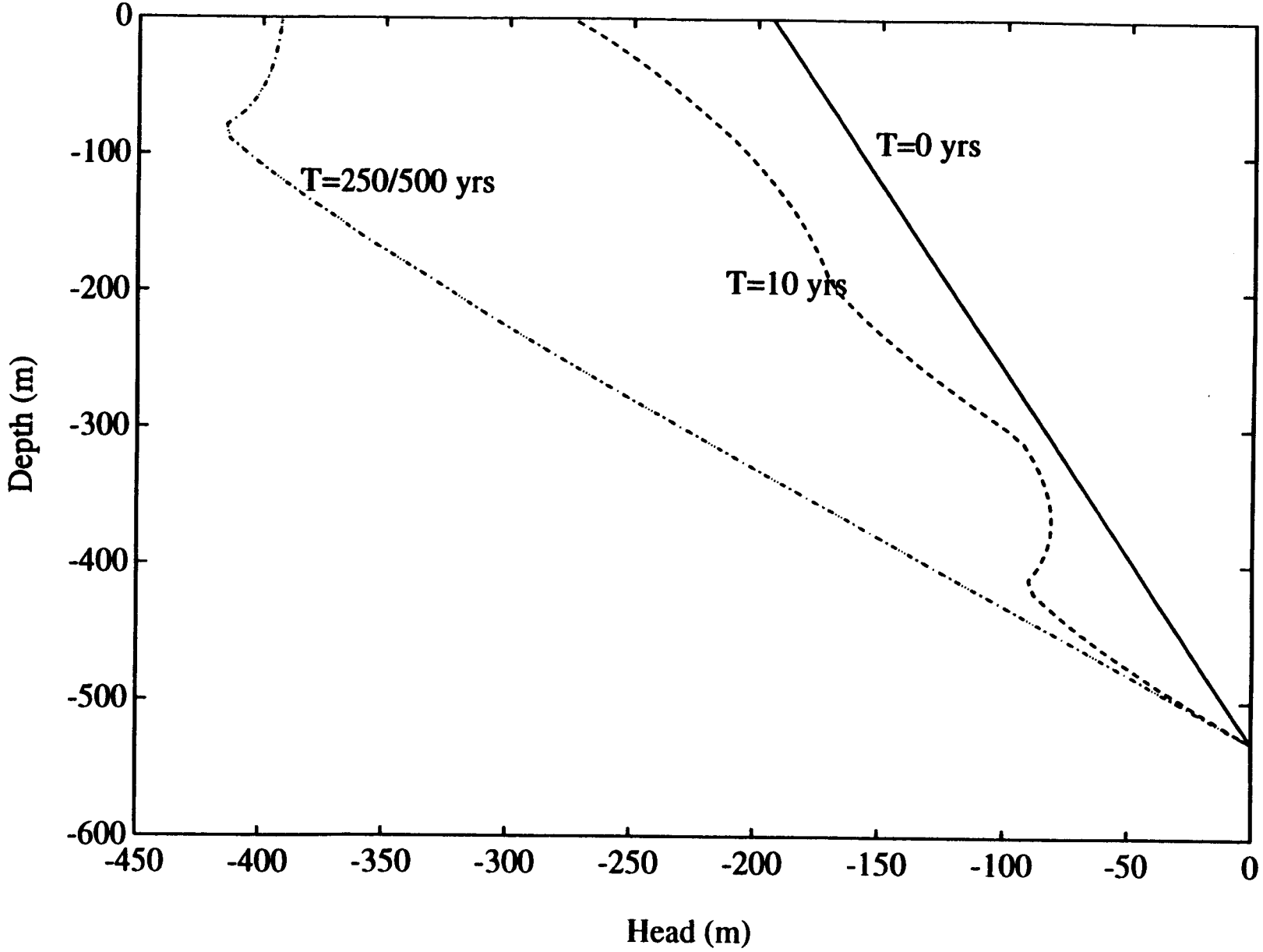

Figure 4-2. Temporal variation of pressure head profile for variation of case 1 with q_0 = 1 mm/year

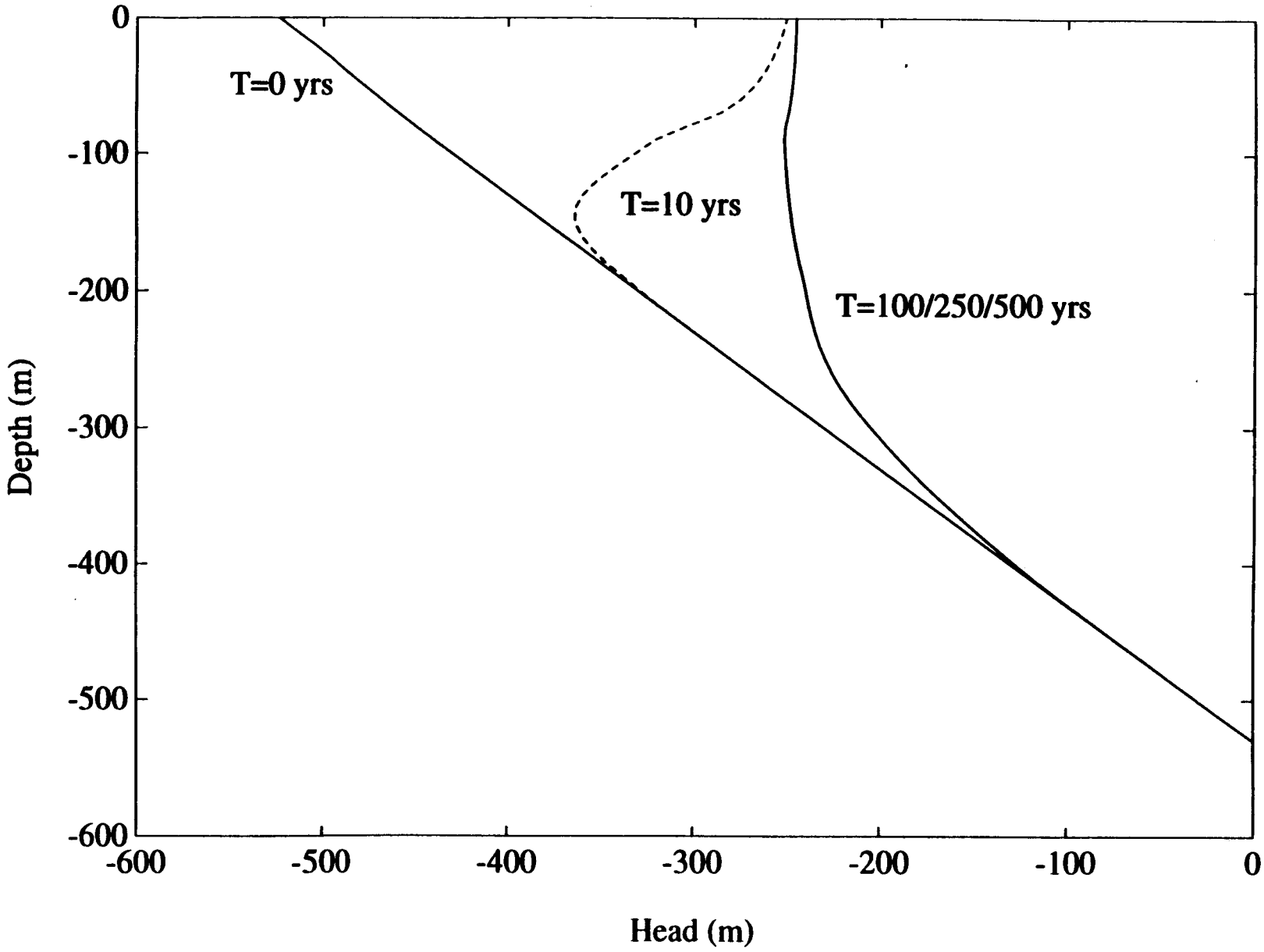

Figure 4-3. Temporal variation of pressure head profile for variation of case 2 with q_0 = 50 mm/year

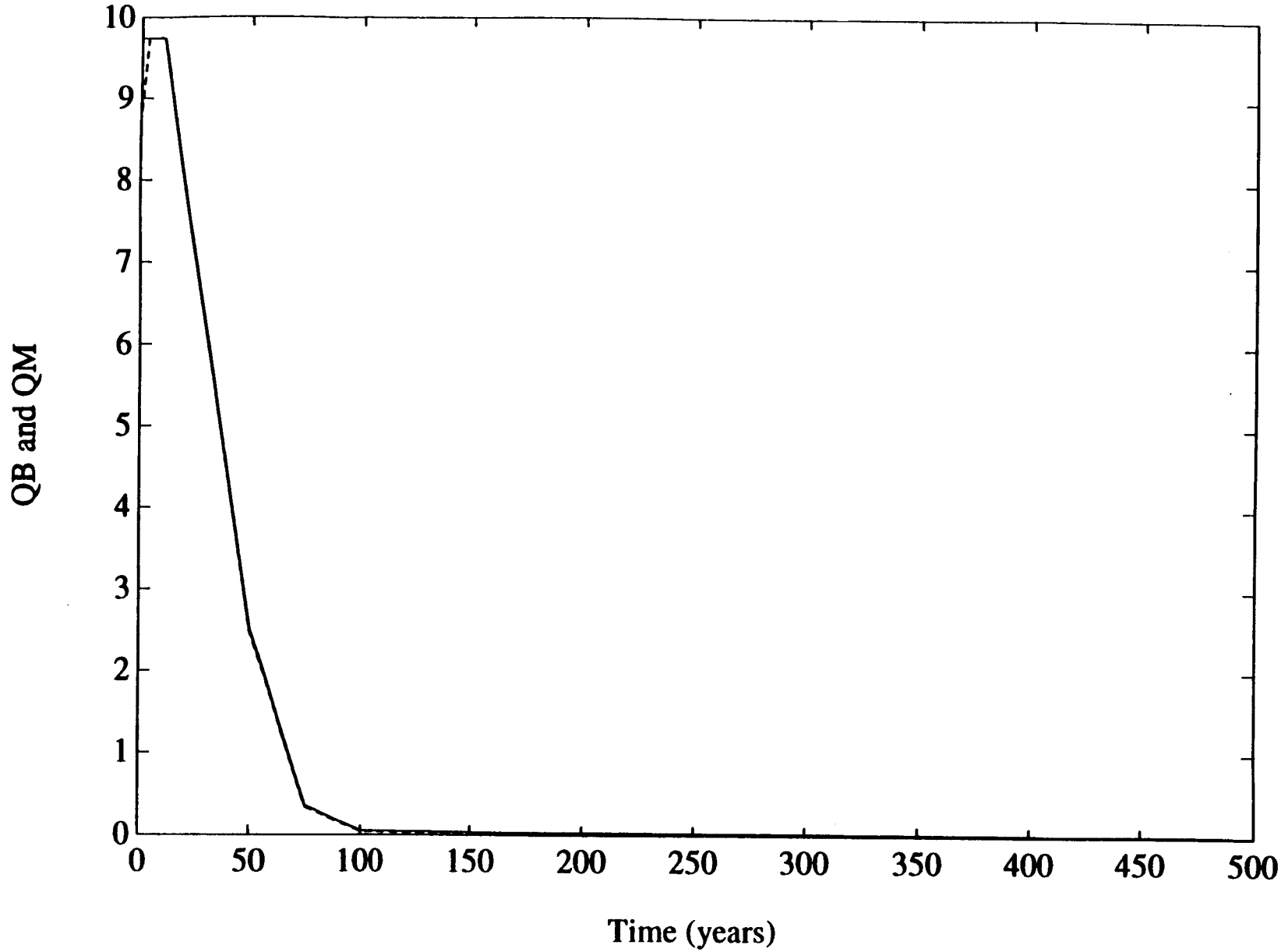

Figure 4-4. Rates of change of total mass, Q_B and Q_M, plotted as a function of time for case 2

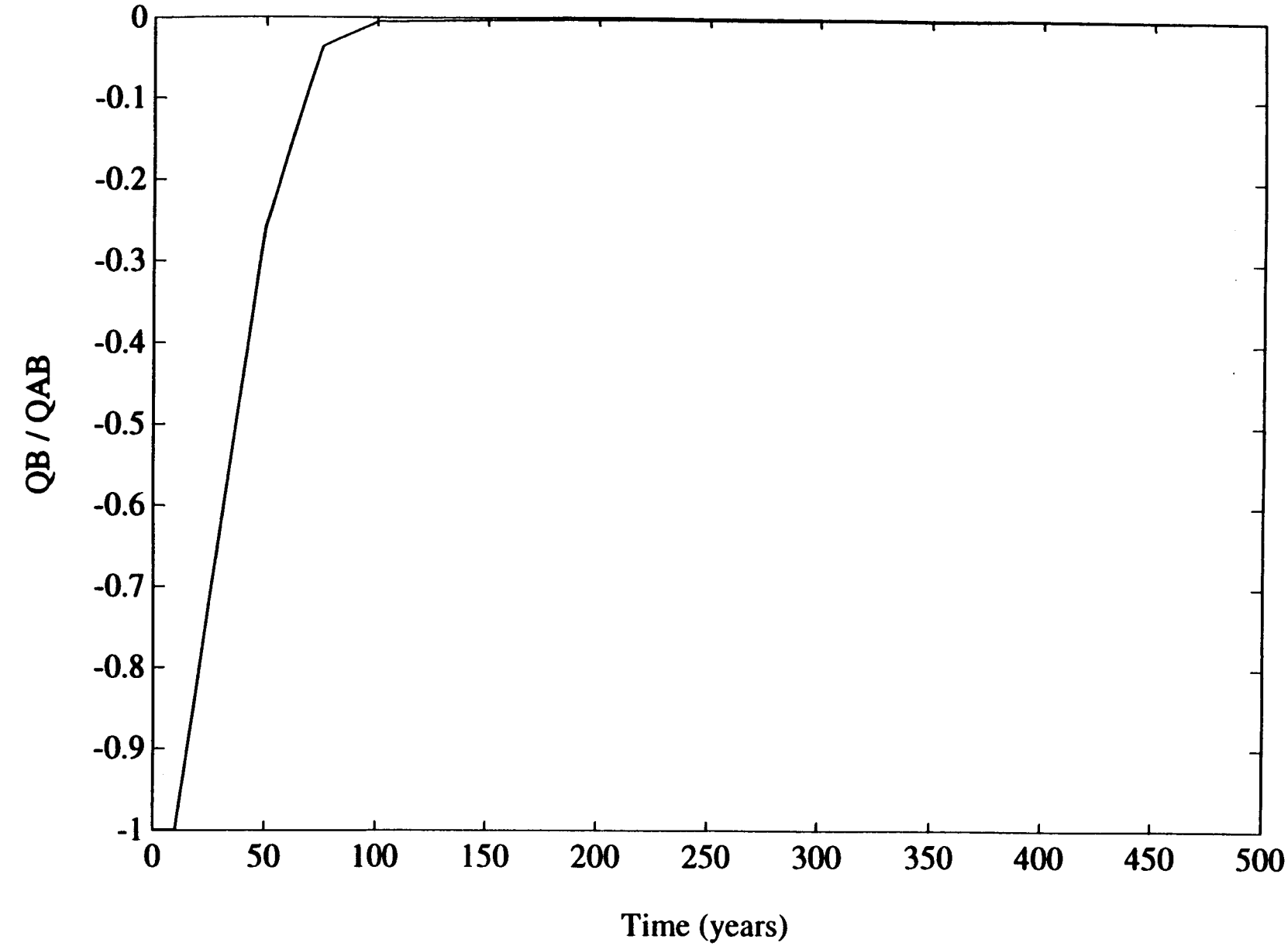

Figure 4-5. Relative measure of rate of change of total mass (ϵ), plotted as a function of time for case 2

$\epsilon = \frac{Q_B}{Max\{Q_i\}}$ as a function of time. Note that the Q_i's (i = 1,...,6) represent the discharge rates through each of the six boundaries (actually labeled A1,B1; A2,B2; and A3,B3 in the BIGFLO code). Figure 4-5 clearly shows that the relative measure $\epsilon(t)$ becomes smaller than 1 percent at $t \approx 100$ years, indicating steady-state.

4.2 FLOW FIELD IN THE PRESENCE OF A FAULT ZONE, BUT NO DIP (CASES 10 AND 20 OF FIGURE 3-9)

Following the successive approximation methodology described in section 3.4, the initial and boundary conditions for the simulations presented in this section are taken from the steady-state results of less complex flow systems. Thus, the complexity of the present system is increased in three ways. First, by incorporating a fault zone in the middle of the domain. Second, by changing the no-flow lateral boundary conditions to non-uniform pressure (Dirichlet) boundary conditions, the latter being obtained from previously simulated steady-state flow fields. Third, by using the prior steady-state results as initial conditions.

To gain some insight into the behavior of this relatively complex flow system, some ancillary simulations have also been conducted. For example, Figure 4-6 depicts the pressure head profile at two transects, one in the middle of the fault zone (node 15) and one very close to the left face boundary (node 3), after 200 years of simulation. The initial condition and boundary conditions for this simulation were obtained from steady-state results for case 2. Two key features of this simulation are that: (i) the net infiltration rate is "turned off" by setting q_o = 0 mm/year, and (ii) some of the fault zone properties [namely β and h_b] are equal to the corresponding matrix layer properties. This way, we re-evaluate and re-emphasize the consistency need described in the previous sections. It can be seen that the "wet" state of the system is incompatible with the hydraulic properties and recharge rate driving the system. Therefore, the fault zone attempts to compensate for this difference by "drying" at the top of the domain and "wetting" at the middle portion of the domain. The effect of layering is clearly apparent in the top-half part of the flow domain. With increasing depth, however, the system is closer to saturation, rendering the effects of layering negligible as far as pressure head distribution is concerned. Finally, it is worthwhile noticing that, outside the immediate neighborhood of the fault zone, the system remains unaltered: compare Case 20 (Figure 4-6) to Case 2 (Figure 4-3).

Figures 4-7 and 4-8 show results from a simulation corresponding to the next level of complexity. This time, while some of the above-mentioned fault-zone properties are still equal to the corresponding matrix properties, the net infiltration rate is set to q_o = 50 mm/year. Again, the time of simulation is 200 years. The pressure profiles shown in Figure 4-7 clearly show that the flow field has been affected by infiltration in a much larger part of the flow domain (vertical transects are shown inside the fault, at the fault-matrix interface, and in the matrix far from the fault). However, no visible changes are detected at depths greater than 150 m, or at distances greater than 50 m away from the fault zone (node 13). Finally, Figure 4-8 presents the temporal variation of the pressure head profile right in the middle of the fault

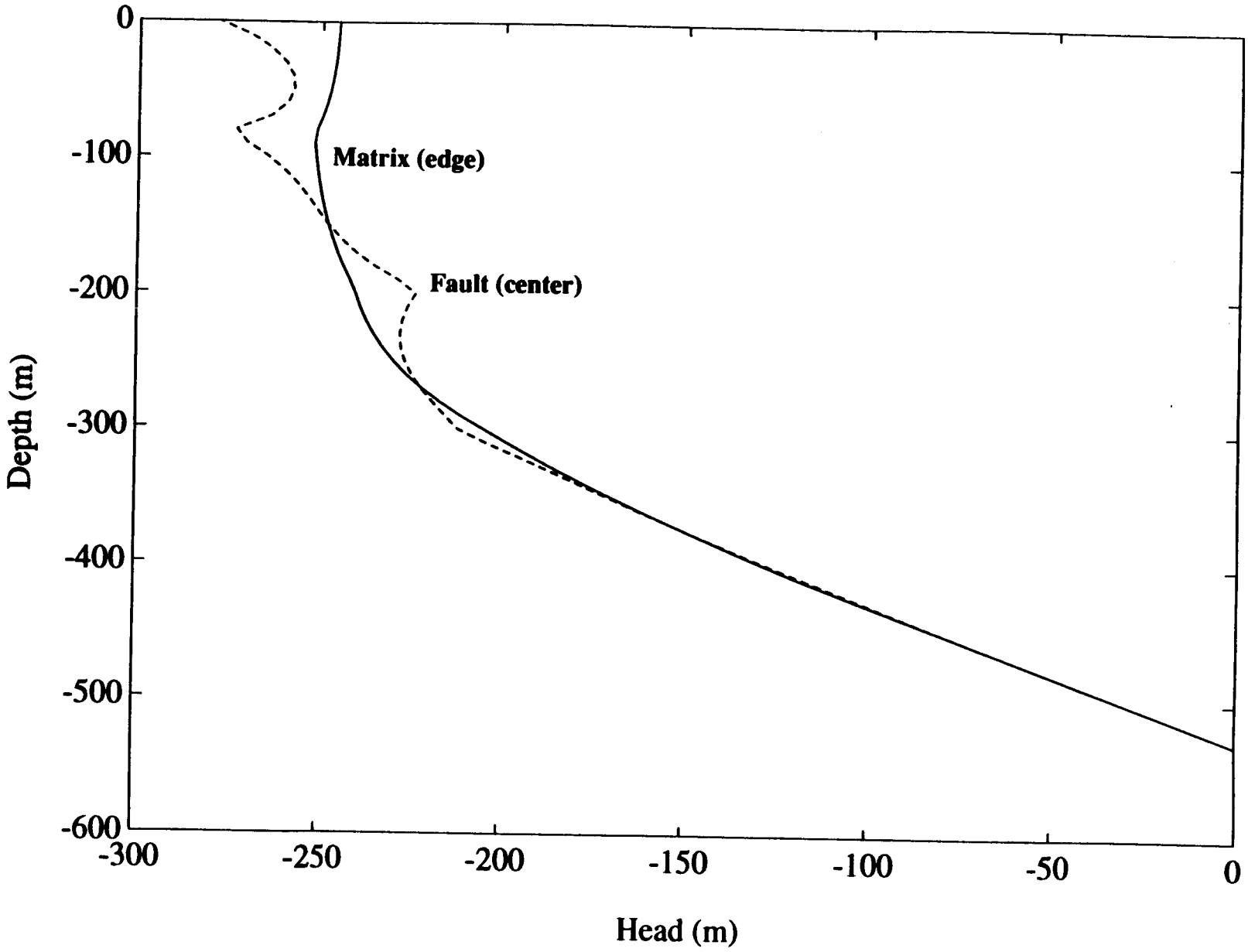

Figure 4-6. Pressure head profile for t = 200 years at two different transects. Scenario is a variation of case 20 with q_o = 0 mm/year and some, but not all, of the fault properties, equal to the rock matrix.

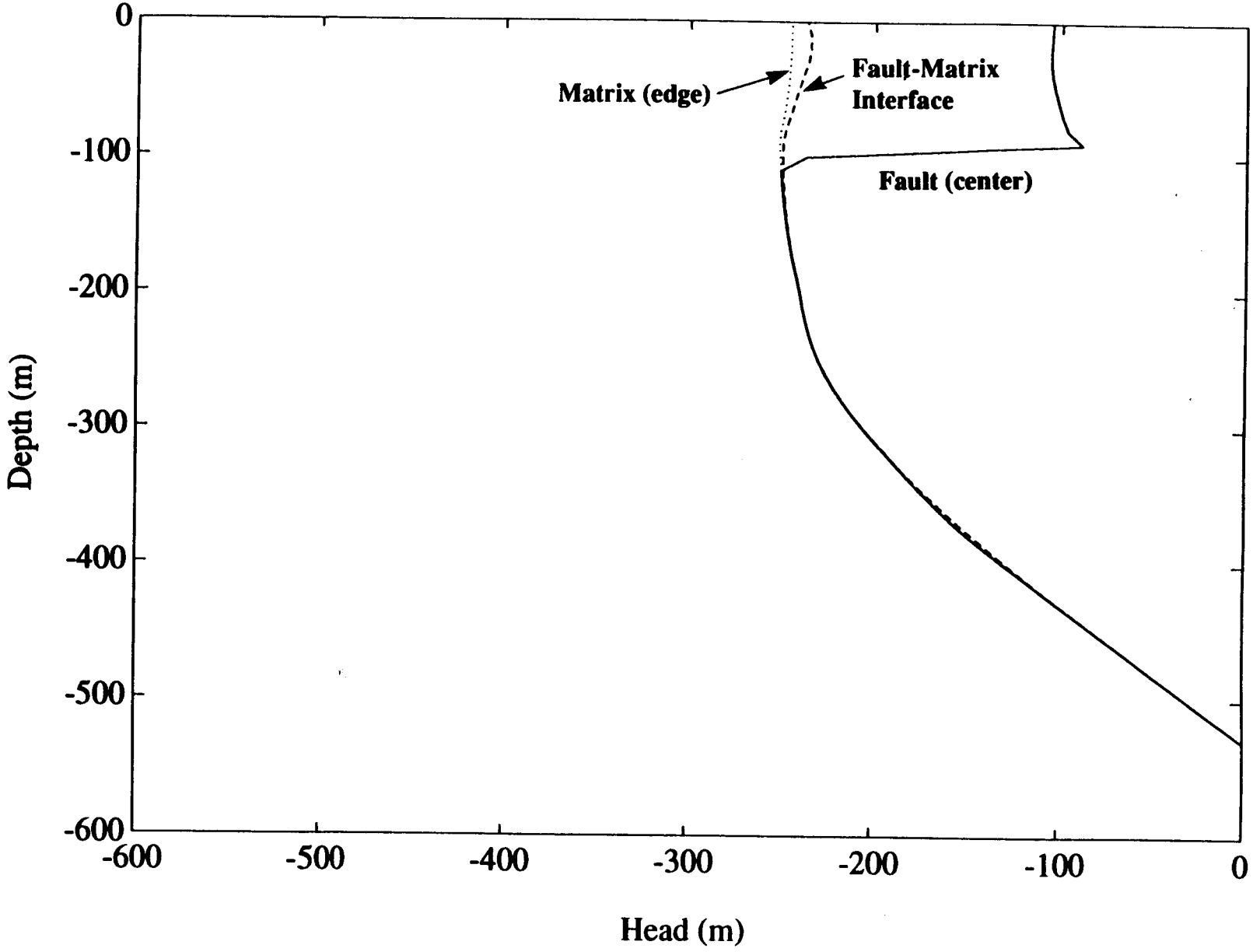

Figure 4-7. Pressure head profile for t = 200 years at three different transects. Scenario is a variation of case 20 with q_o = 50 mm/year, and some, but not all, of the fault properties equal to the rock matrix.

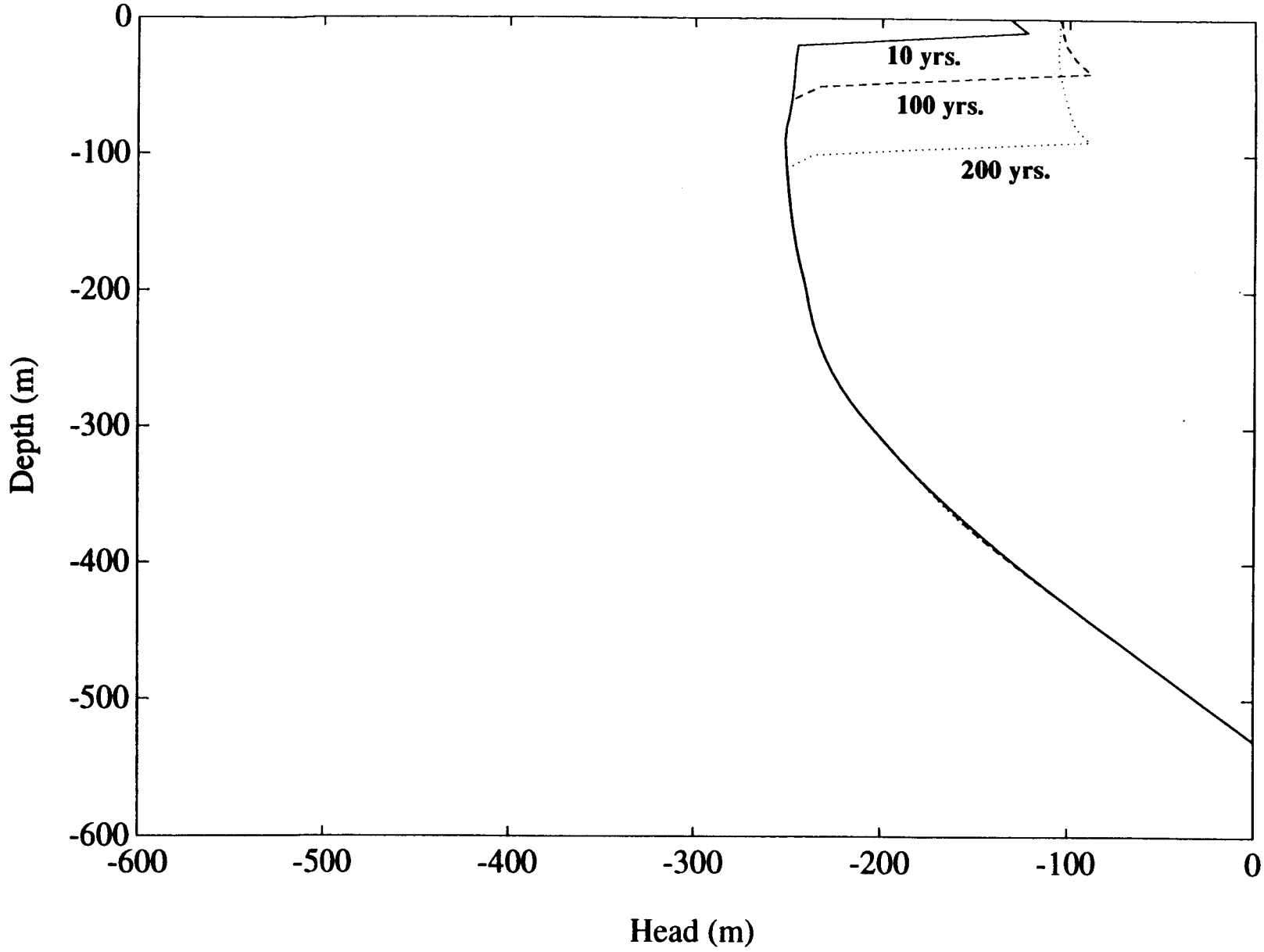

Figure 4-8. Temporal variation of pressure head profile in the middle of the fault zone. This case is a variation of case 20 with q_0 = 50 mm/year, and some, but not all, fault properties equal to the rock matrix.

zone (node 15). The pressure in the fault is considerably higher (wetter) than in the neighboring rock matrix, and a very sharp wetting front can be seen to migrate down the fault. However, the fault remains unsaturated at all times, the pressure in the fault being less than its assumed air entry pressure.

The next level of complexity in the flow system involved simulations corresponding to case 20, where q_o = 50 mm/year and the fault zone is characterized by the hydraulic parameters found in Table 3-1. Again, the initial and boundary conditions are extracted from steady-state results of simulations for case 2. Figure 4-9 depicts results of this simulation at time t = 120 years, both as a pressure head contour plot and vertical transects at different locations within the flow domain. The contour plot indicates that the effects of infiltration are "felt" by a region having the same lateral extent as in the previous simulations (about 100 m on either side of the fault). The infiltration "signal", however, is affecting a greater depth, down to almost 400 m. In Figure 4-9, the vertical pressure profiles are presented at different horizontal locations: node 15 is in the middle of the fault zone, node 14 is located at the interface between matrix-fault, and node 13 is away from the fault, 50 m into the rock matrix.

Figure 4-10 is similar to Figure 4-9; it depicts vertical pressure head profiles at the same locations, and presents also the temporal variation of these profiles (times 10, 60, and 120 years). It can be seen that at node 3, which is located far away from the fault zone, no transient effects are detected at any time. Node 13 senses the effect of the fault, but with very minor temporal variations. Finally, nodes 14 and 15 exhibit the most severe temporal variation, reaching fluctuations in pressure head of up to 100 m. It should be noted that no temporal trend can be detected, since the pressure head front seems to be oscillating with time. This behavior will be described in detail later in this section.

In Figure 4-11, the early time behavior of the flow system is presented in the form of contour plot snapshots, at times of 1, 2, 4, and 8 years of simulation. It is interesting to observe how the moisture front (as indicated by higher pressure values) propagates downward in the fault zone, and to a lesser degree laterally in the rock matrix. To explore further this transient approach to a steady-state, temporal variations of pressure head profiles in the middle of the fault, are presented in Figures 4-12a, b, and c. It can be seen that, after the initial transients during the period 0-10 years, the system experiences an oscillatory behavior thereafter. No trend to a stable steady-state can be detected; the pressure head seems to fluctuate quasi-periodically around an approximate mean value of -100 m.

The mass balance measure of net flow rate through the system, $\epsilon(t)$ [described previously] is plotted in Figure 4-13. Note that this measure, apart from the very early times $t < 1$ year, appears to fluctuate quasi-periodically between $\pm$ 2%. This behavior supports prior observations regarding the pressure head profile fluctuations. Similar behavior is depicted in Figure 4-14, where the net discharge rate through boundaries, Q_B, and the rate of change of total mass, Q_M, are plotted as a function of time. Note that it takes about 80 years for $Q_B(t)$ to become nearly indistinguishable from $Q_M(t)$. This indicates that numerical mass balance errors become insignificant after $t \approx 80$ years. Nonetheless, even where $Q_B(t) \approx Q_M(t)$, the two rates exhibit oscillatory behavior, consistent with all other results presented so far.

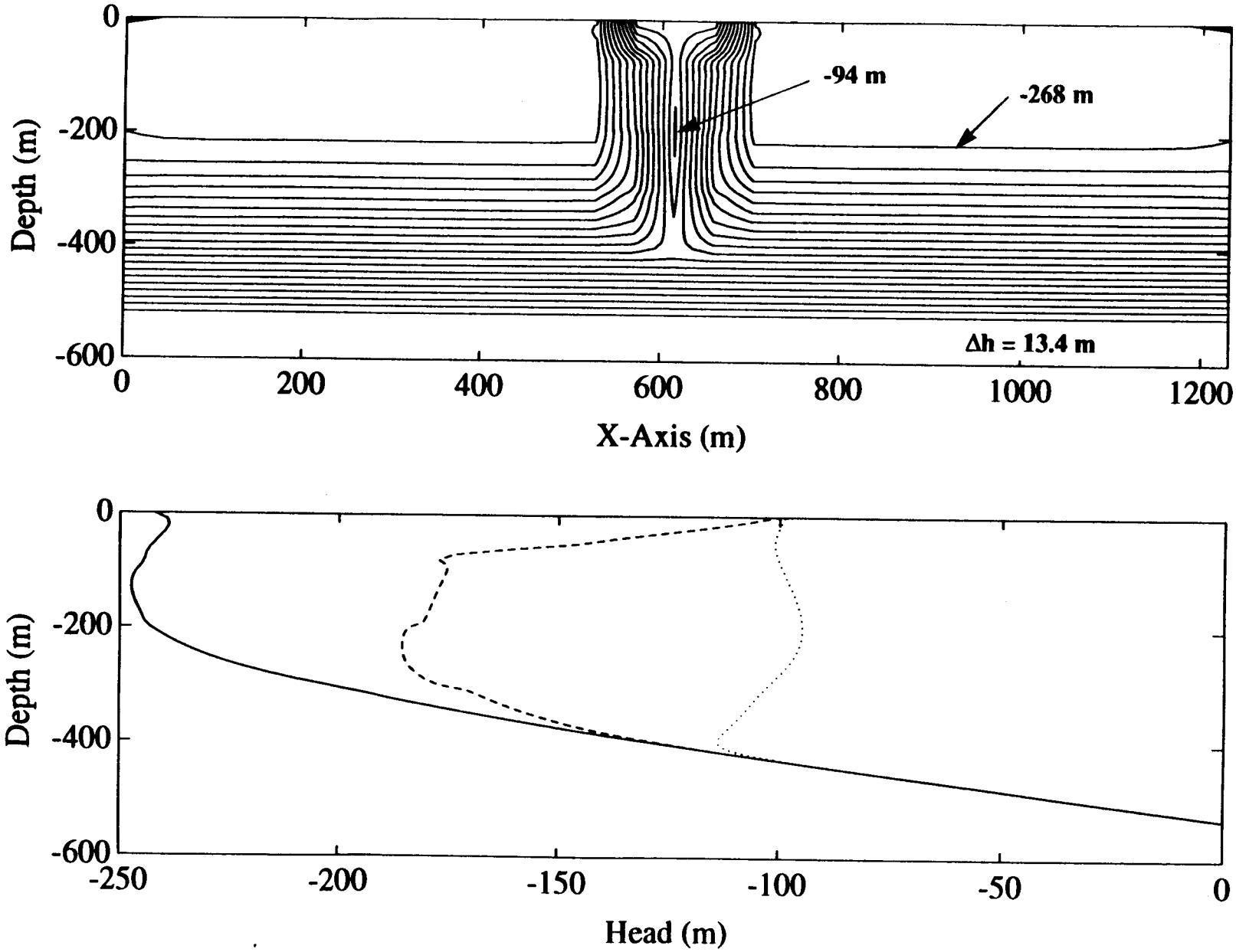

Figure 4-9. Pressure head results for t = 120 years and case 20. Above: Contour plot is vertical cross-section at Y = 40 m. Below: Profile at three different transects. Dotted line: Fault (center); Dashed line: Fault-matrix interface; Solid line: Rock matrix (edge).

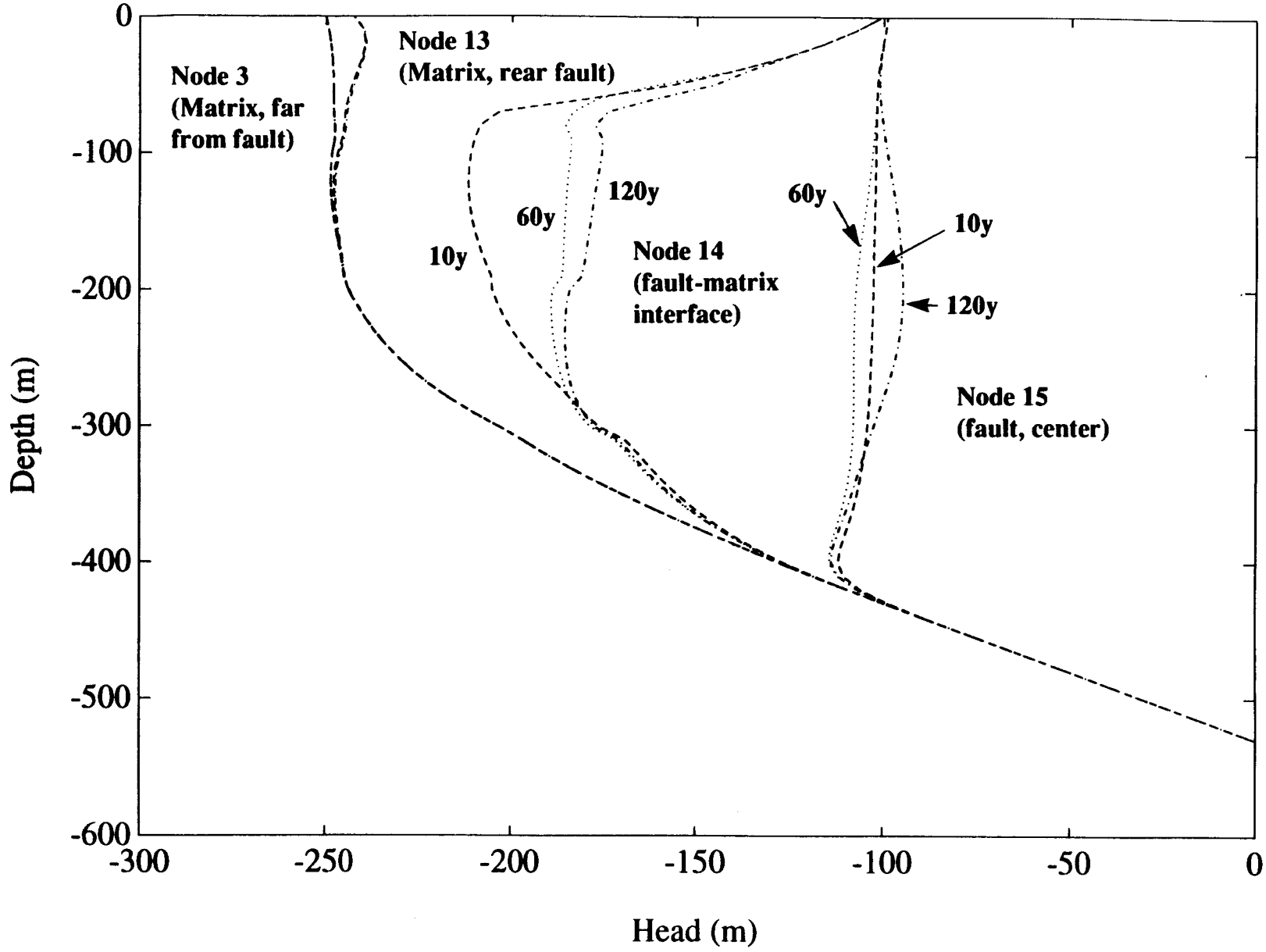

Figure 4-10. Temporal and spatial variation of pressure head profiles for case 20 at time t = 120 years

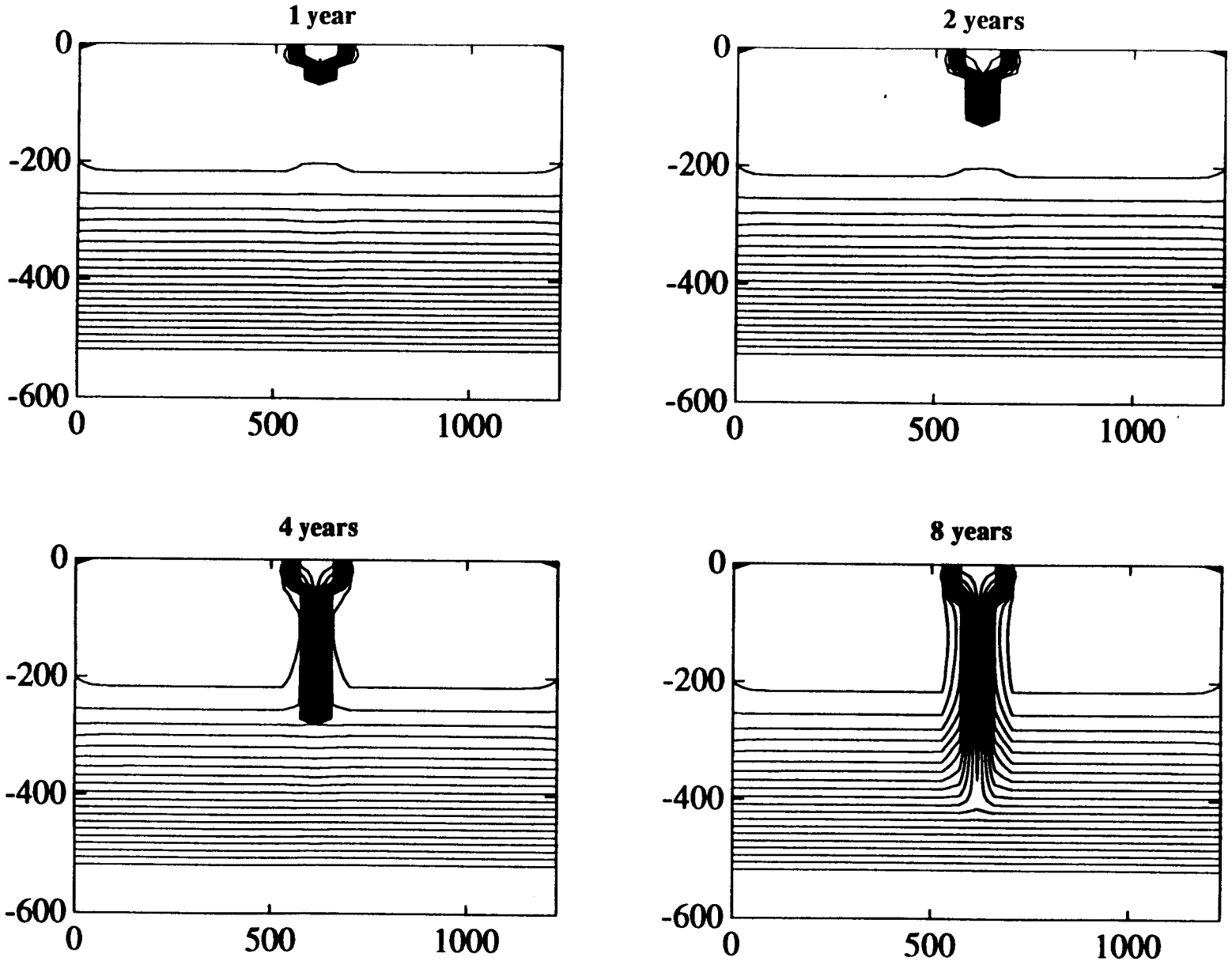

Figure 4-11. Propagation of moisture at early times for case 20 at times t = 1, 2, 4, and 8 years

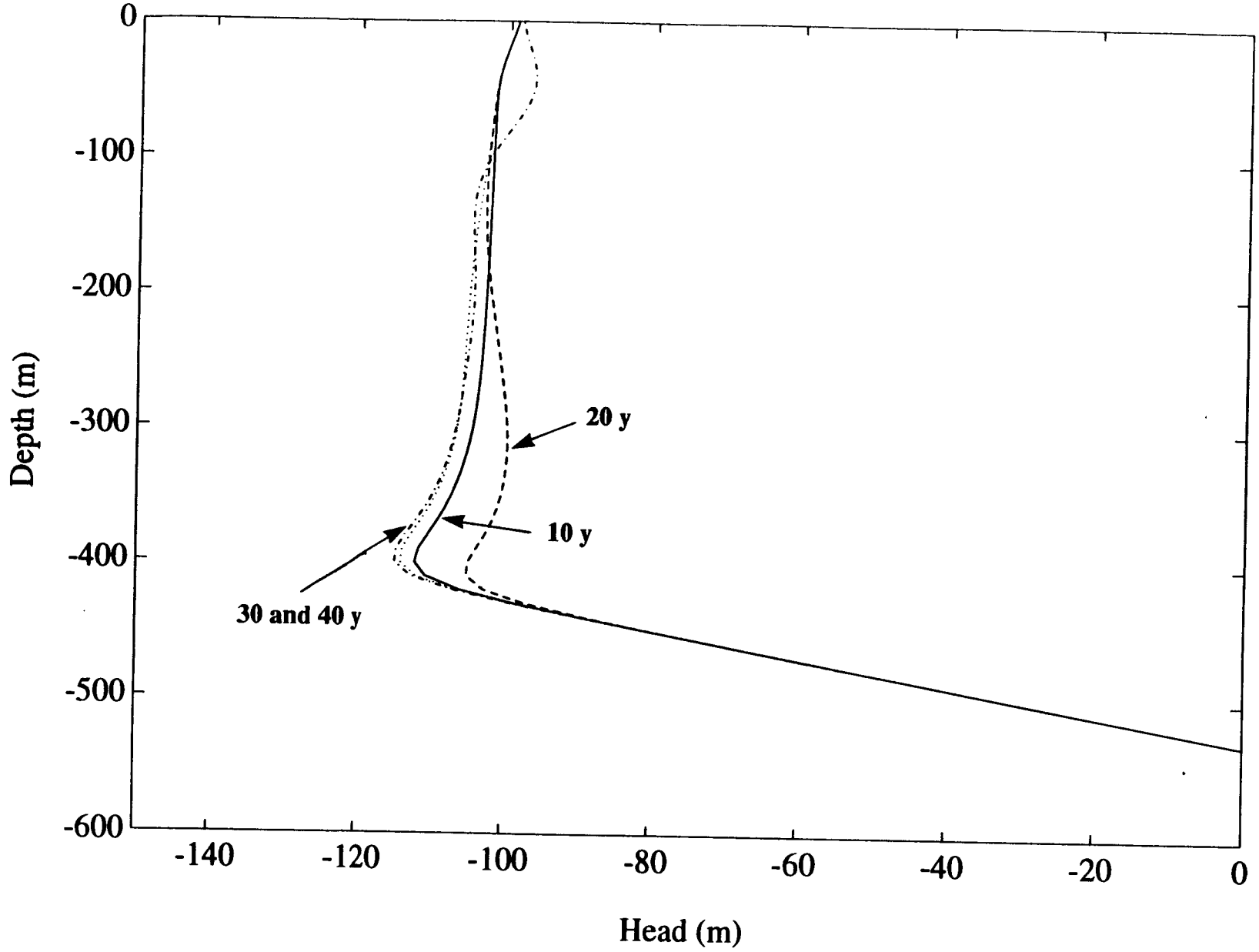

Figure 4-12a. Temporal variation of pressure head profile in the middle of the fault for case 20: $0 < t \leq 40$ years

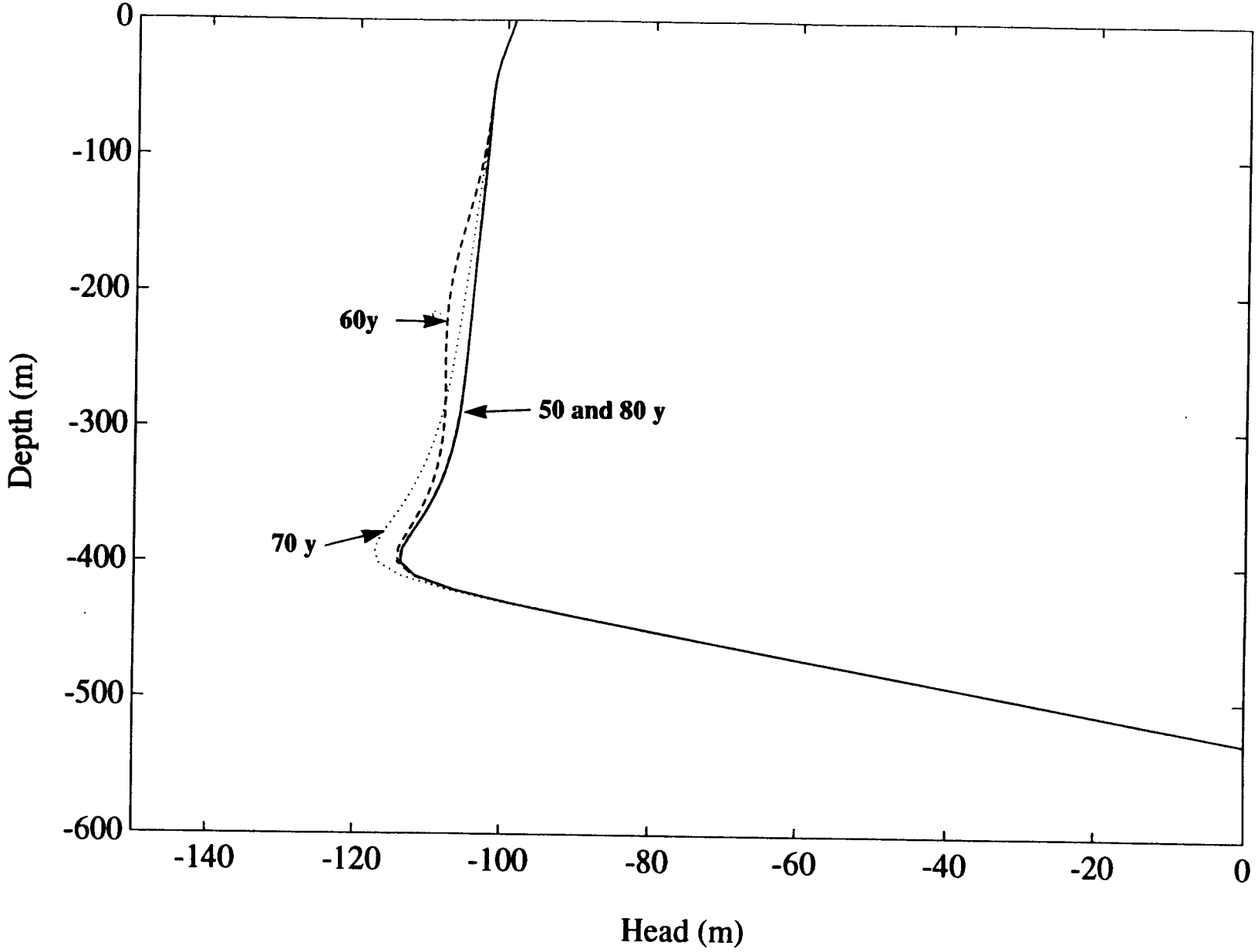

Figure 4-12b. Temporal variation of pressure head profile in the middle of the fault for case 20: 50 ≤ t ≤ 80 years

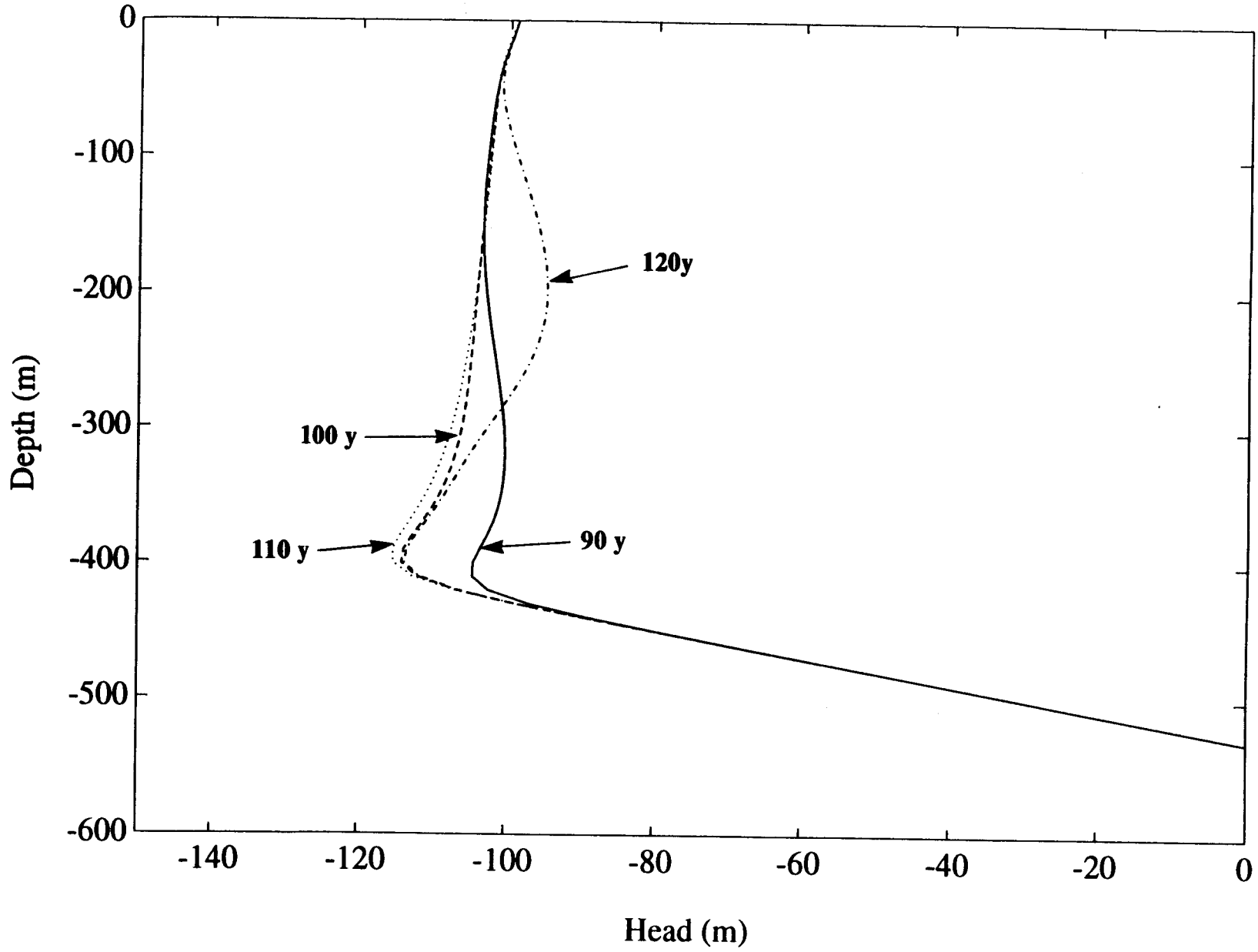

Figure 4-12c. Temporal variation of pressure head profile in the middle of the fault for case 20: 90 ≤ t ≤ 120 years

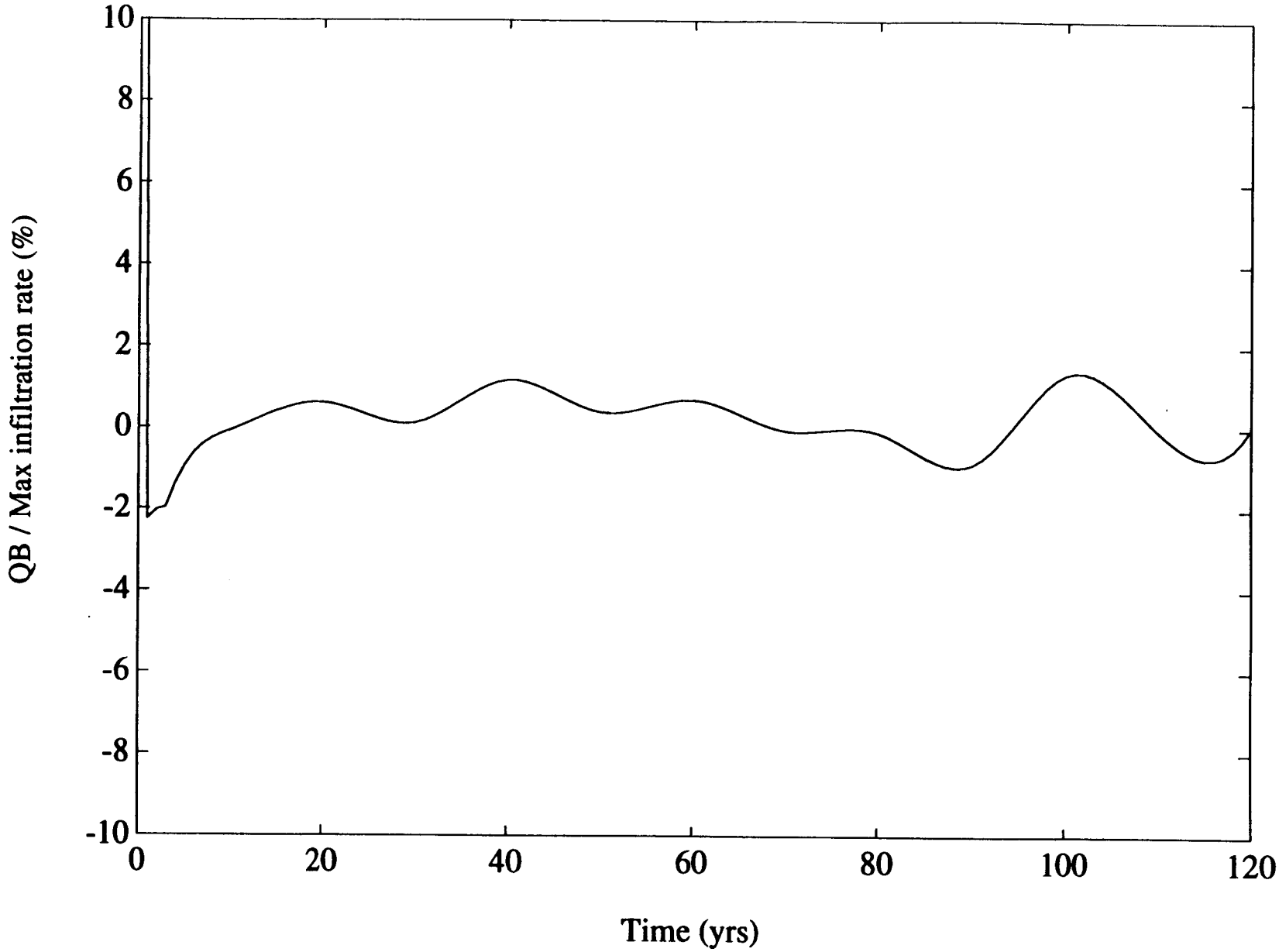

Figure 4-13. Relative measure of rate of change of total mass (ϵ), plotted as a function of time for case 20

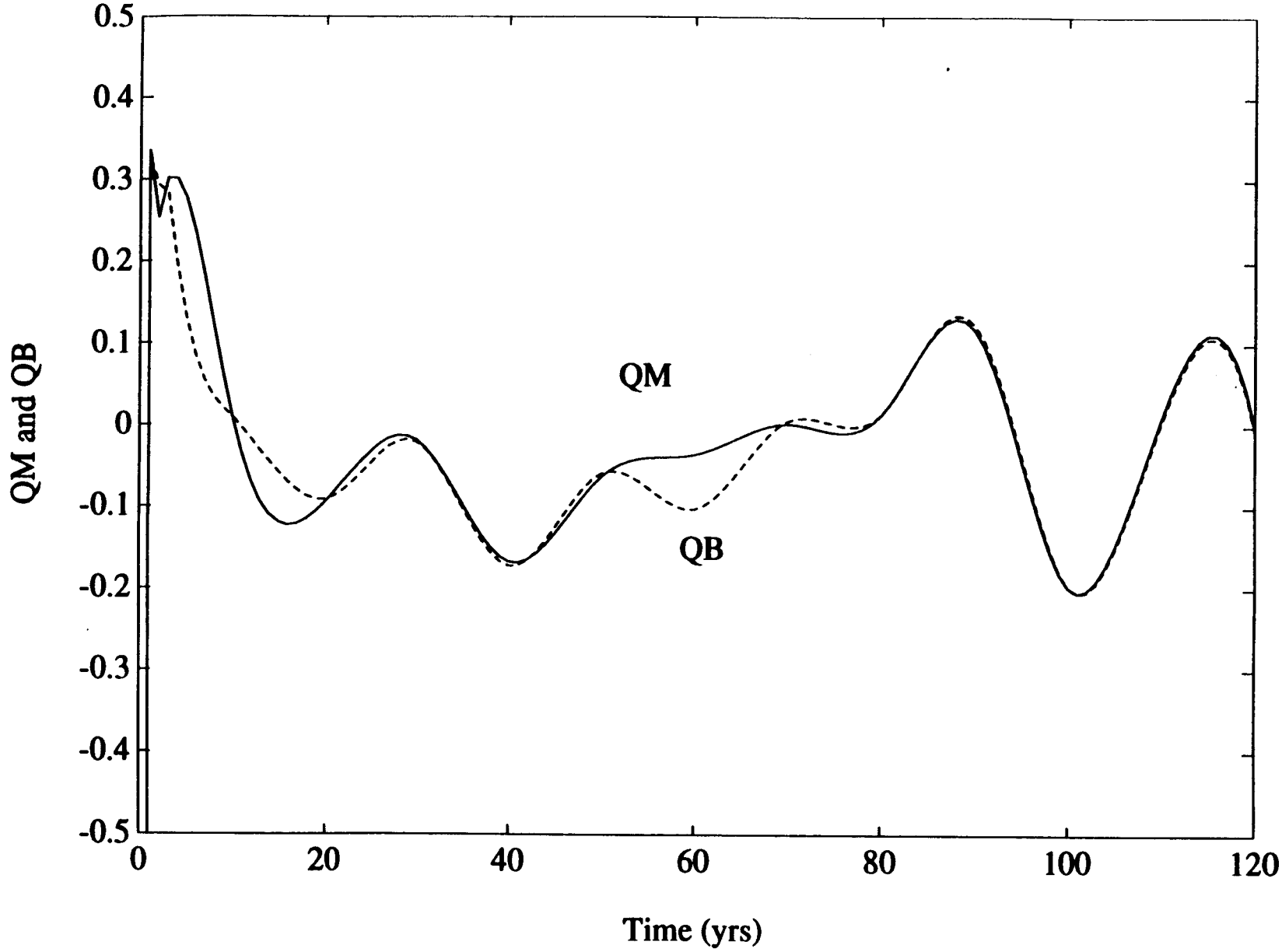

Figure 4-14. Rates of change of mass, Q_M and Q_B, versus time for case 20

The final set of simulations was a variation of case 10 (q_0=0 mm/year and fault), the only difference being that the initial and boundary conditions are taken to be the steady-state pressures of case 2 (q_0=50 mm/year and no fault). The reason for selecting this variant is two-fold. First, there is interest in observing how the flow domain becomes "dry" in conjunction with the fault presence. Second, it is of interest to observe how the system behaves in the case where a very "wet" hydroclimatic period is followed by an extremely "dry" hydroclimatic period. Figure 4-15a shows the contour plot of pressure head after 500 years of simulation (steady-state). Note the inertia which the system exhibits. Only the top 200 m of soil have "dried" out.

Interestingly enough, as depicted in both Figures 4-15a and 4-15b, the fault zone remains wetter than the rock matrix in the top 200 m. This is probably due to the fact that the matrix is more conductive than the fault, and that the matrix drains more easily than the fault, in this particular suction range (250-300 m of suction). See earlier discussion of conductivity crossing points around Figures 3-3 and 3-4.

4.3 FLOW SYSTEM WITH LAYERS, FAULT ZONE, AND DIP ANGLE (CASES 100 AND 200 OF FIGURE 3-9)

The final level of complexity in the flow system involved simulations corresponding to case 200, with five layers, a fault zone, a dip, a high infiltration rate q_o = 50 mm/year, and initial-boundary conditions given by steady-state pressures corresponding to the case 2 simulation (same, but without fault nor dip). Compared to the previous sub-section, the flow system is now under the influence of a modified gravity vector, so that the dip angle of 6 degrees to the East is emulated.

Figure 4-16 presents results in the dipped and faulted system after 120 years of simulation. It should be observed that the previous symmetry in the pressure head contours is destroyed, and that the matrix is slightly "wetter" in the East side of the flow domain. This is also seen in Figure 4-16b where pressure head profiles at five different vertical transects are depicted. While the results are not substantially different from those presented in section 4-2, the East nodes 17 and 16 are indeed slightly "wetter" than the West nodes 13 and 14, respectively. The reader should be reminded that node 15 is in the middle of the fault zone, nodes 14 and 16 are at the fault-matrix West and East interfaces, respectively, and nodes 13 and 17 are 50 m in the rock matrix to the West and East of the fault, respectively.

Figure 4-17 shows the temporal behavior of the pressure head profile for a transect located in the middle of the fault. Oscillatory behavior is clearly observed, with one difference compared to the no-dip case. There seems to be a less "noisy" fluctuation of pressure around its mean value (over time). This observation is consistent with the mass balance information depicted in Figures 4-18 and 4-19. In both figures, the "amplitude" of fluctuation is significant but somewhat smaller, when compared to the respective Figures 4-13 and 4-14 for the no-dip case.

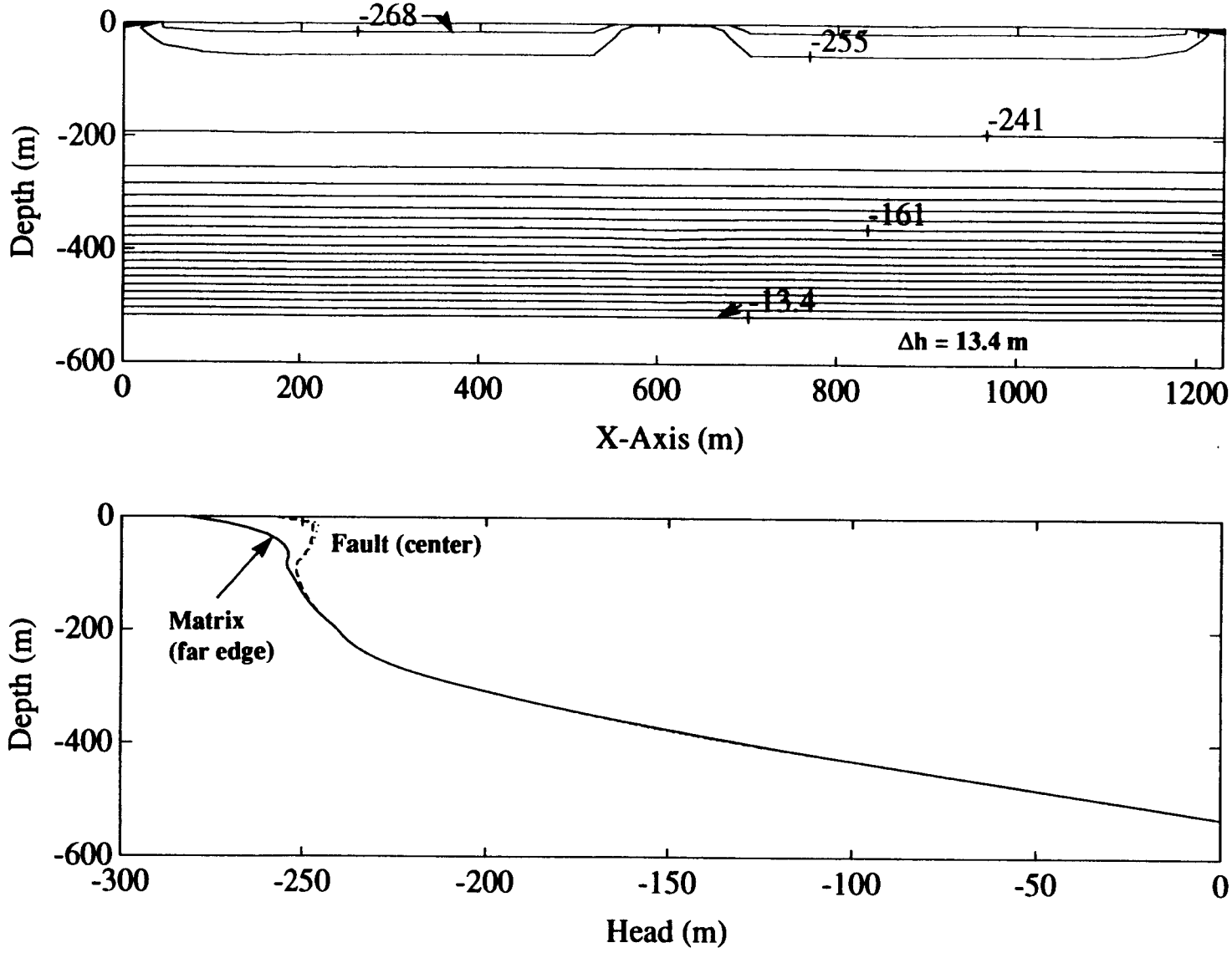

Figure 4-15. Pressure head results for t = 500 years. Case is a variation of case 10 (q_o = 0 mm/year, with a fault) with initial-boundary conditions from case 2 (q_o = 50 mm/year, without a fault). Above: Contour plot at plane Y = 40 m. Below: Profile at different transects. The isovalues of pressure in the contour plot are given with increment Δh = 13.4m.

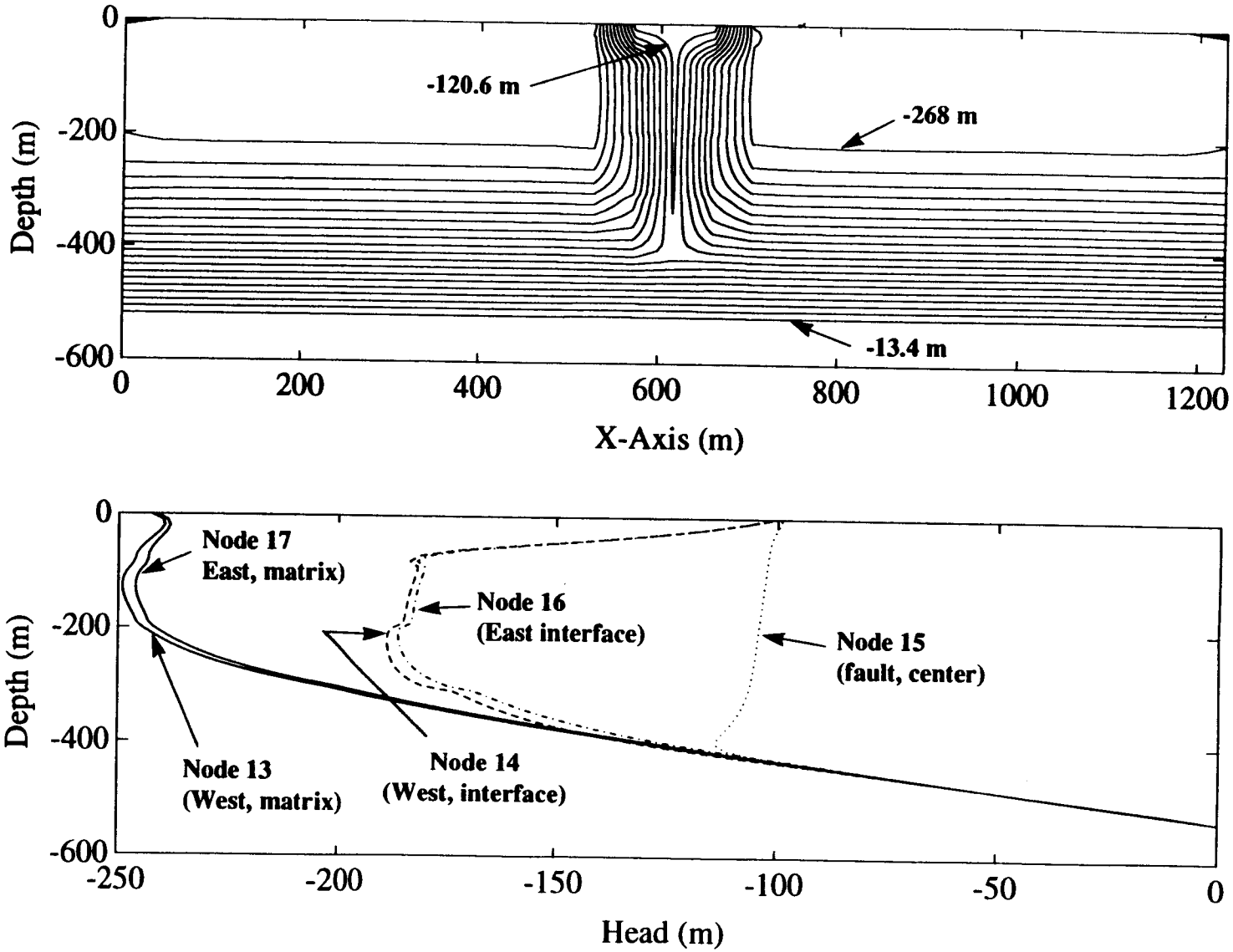

Figure 4-16. Pressure head results for t = 120 years and case 200. Above: Contour plot at plane Y = 40 m. Below: Profiles at five different transects.

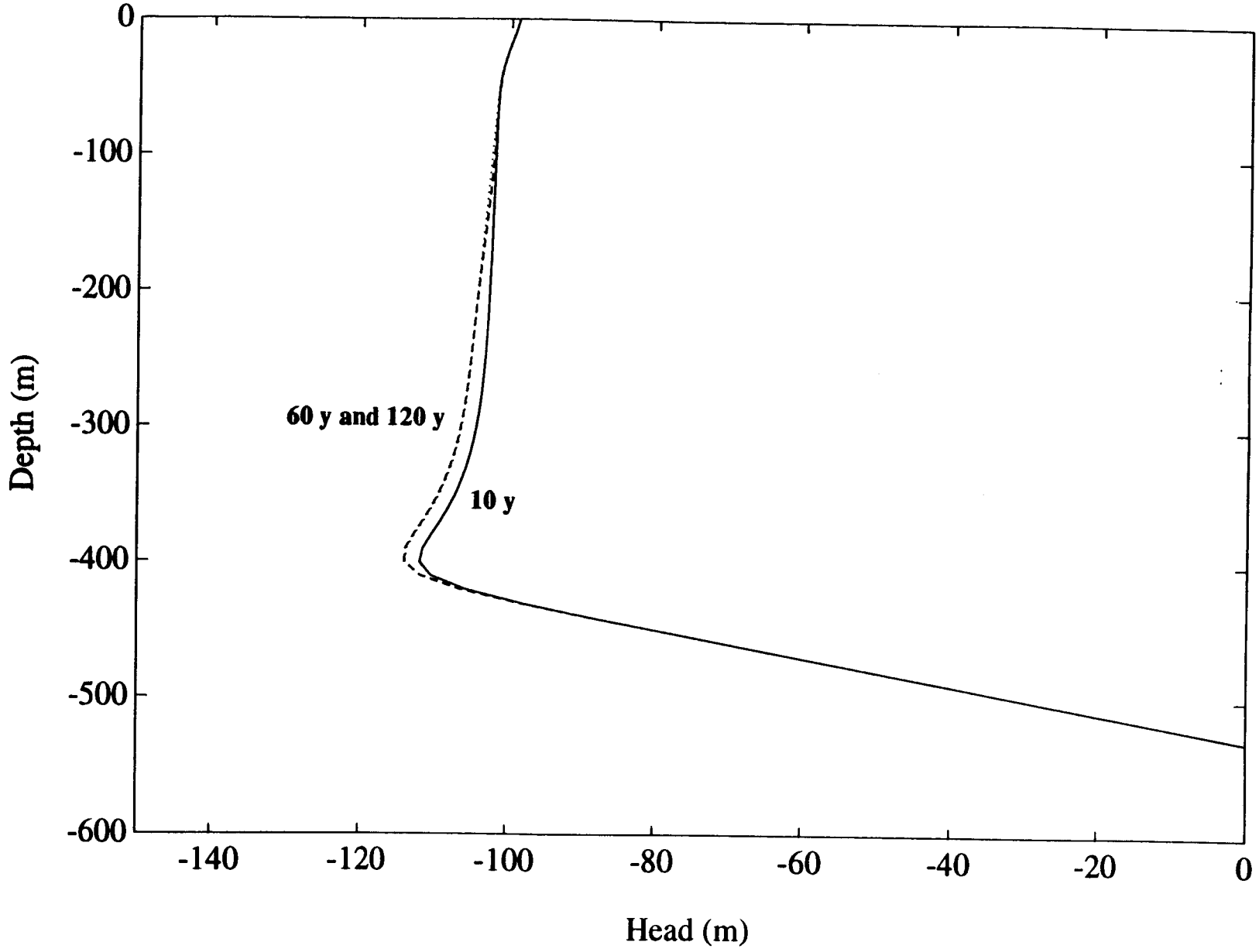

Figure 4-17. Temporal variation of pressure head profile in the middle of the fault for case 200

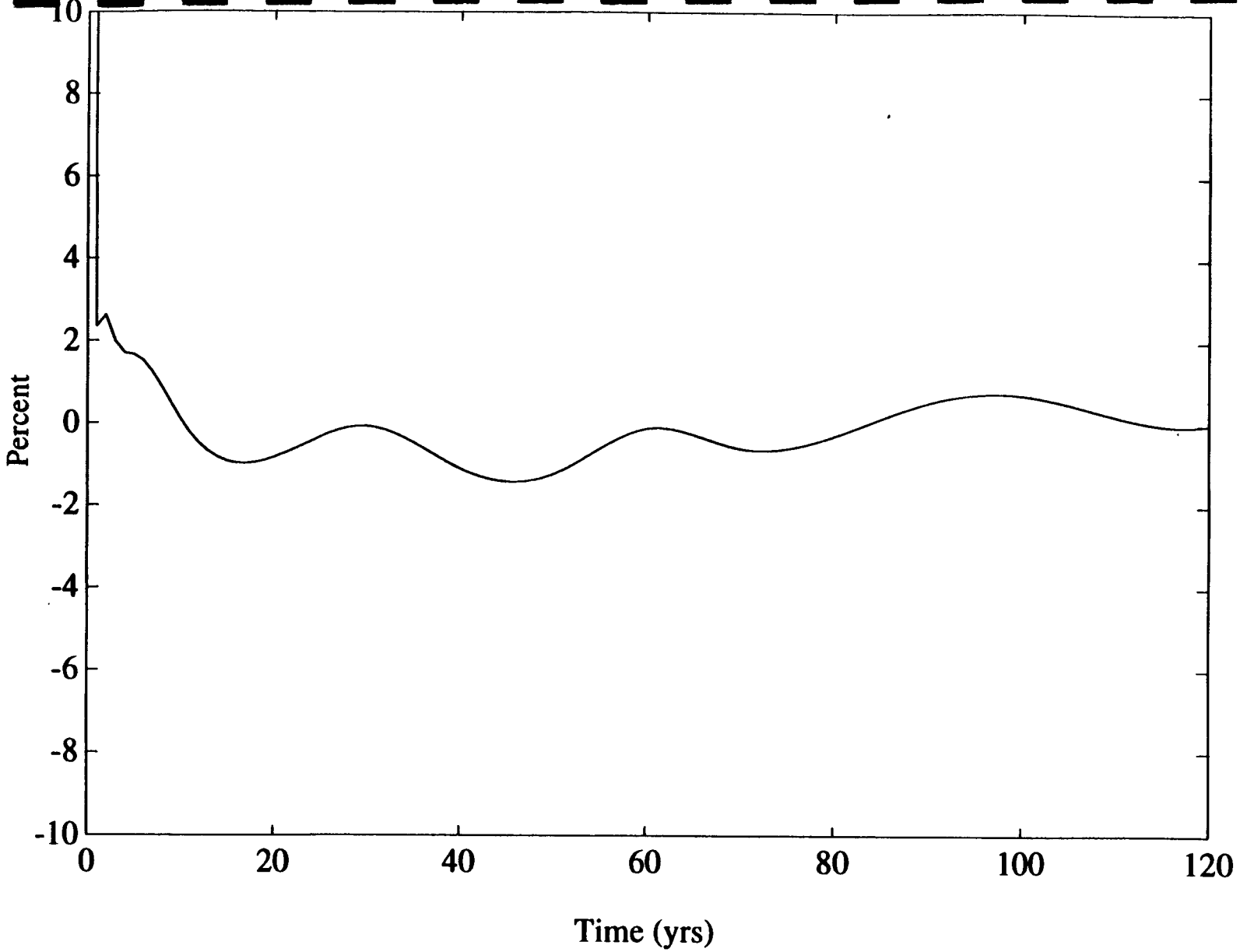

Figure 4-18. Relative measure of rate of change of total mass (ϵ), plotted as a function of time for case 200. In the case at hand, ϵ represents net discharge rate through the system, normalized by the infiltration discharge rate from the top boundary.

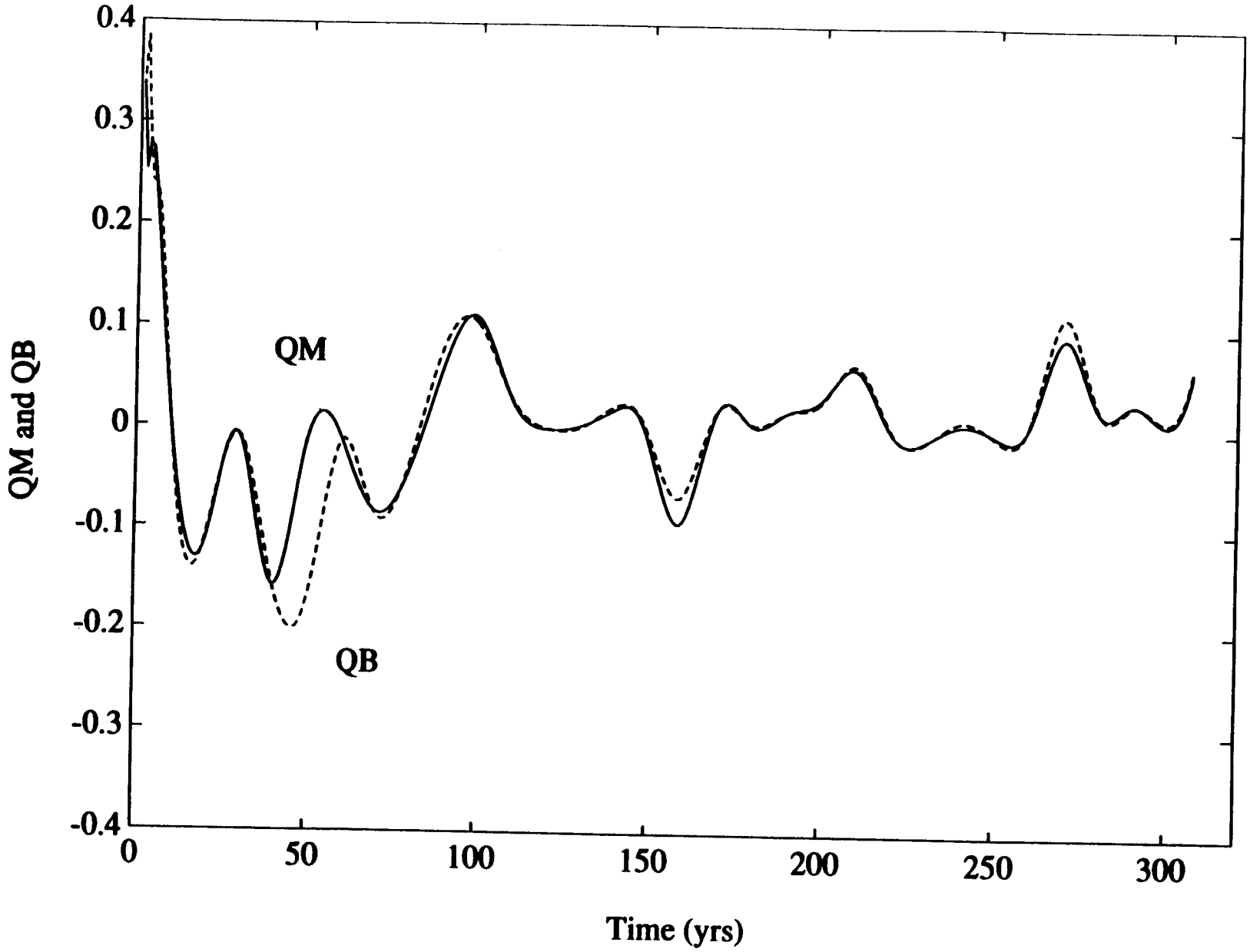

Figure 4-19. Mass balance measures versus time for case 200. Measures plotted are the net discharge rate rates Q_B (t), and the net rate of change of total mass, Q_M (t). The two curves must coincide in the absence of numerical errors.

Note that the simulation was conducted for a time period of more than 300 years. This longer time period was deemed necessary to investigate the existence of periodicity in the observed oscillatory behavior. A discrete Fast Fourier Transform (FFT) analysis was applied to the time series, Q_M (t), starting from t = 51 years. Results of this analysis are presented in a power spectrum plot in Figure 4-20. Three dominant frequencies are observed, f_1 = 0.016 Hz, f_2 = 0.032 Hz, and f_3 = 0.048 Hz, corresponding to a prevailing period $T_1 \approx 60$ years, a secondary period $T_2 \approx 30$ years, and a tertiary period $T_3 \approx 15$ years. Shorter periods exist but have insignificant contribution to the frequency spectrum.

The mechanism that governs this late-time oscillatory behavior may be related to the existence of a crossing point in the hydraulic conductivity curves of the matrix and fault, respectively [see Figures 3-3 and 3-4, and Ababou (1991a) Chap. 5, Figure (5-7)]. This point, physically located near the water table in the case at hand, may act as a "valve" that is turned on or off. Tentatively, these on-off events would take place when the fault becomes "wet" enough to conduct more water than the surrounding rock matrix and vice versa. For instance, the "conductive" fault may become dryer after some time, and the conduction process would then be taken over by the surrounding matrix. In any case, this process seems to be localized along the fault plane Y-Z and in its neighborhood.

Further investigation reveals that the vertical movement of water, oscillatory as it may be, does not significantly contribute to the observed oscillations of net discharge rate through the system. Rather, it is the horizontal movement of water to and from the North-South boundaries that has the most significant contribution. Figure 4-21 depicts the temporal variation of the lateral outflow along the North-South direction. While the "amplitude" of fluctuations of the (net) lateral flow is only 0.0254, or less than 0.5 percent of the mean (net) lateral flow, the corresponding volumes of water discharged to and from the North-South boundaries are mainly responsible for the oscillatory behavior observed earlier in the mass balance plots (rate of change of total mass in the system).

In order to ascertain that the large-time oscillations are not entirely due to numerical instability, we have compared in Figure 4-22 the numerical and physical fluctuations of total mass, in terms of rate of change of mass or net discharge rate through the system. Thus, we defined, in addition to the relative measure of rate of change of mass $\epsilon(t)$, a relative measure of numerical error

$$\eta(t) = \frac{Q_M(t) - Q_B(t)}{\mathrm{Max}|Q_i|} \quad . \tag{4-1}$$

Recall that $\mathrm{Max}|Q_i|$ represents the largest discharge rate through any boundary. In the case at hand, this occurs at the ground surface, with Q=9.7485 m^3/day corresponding to q_0=50 mm/year. Figure 4-22 clearly shows that $|\epsilon(t)|$ remains significantly larger than $\eta(t)$ for t $\geq$ 80 years. Therefore, the large-time oscillations must be assumed to be related to an intrinsic instability of the flow system, rather than to numerical instability alone. It is possible, for

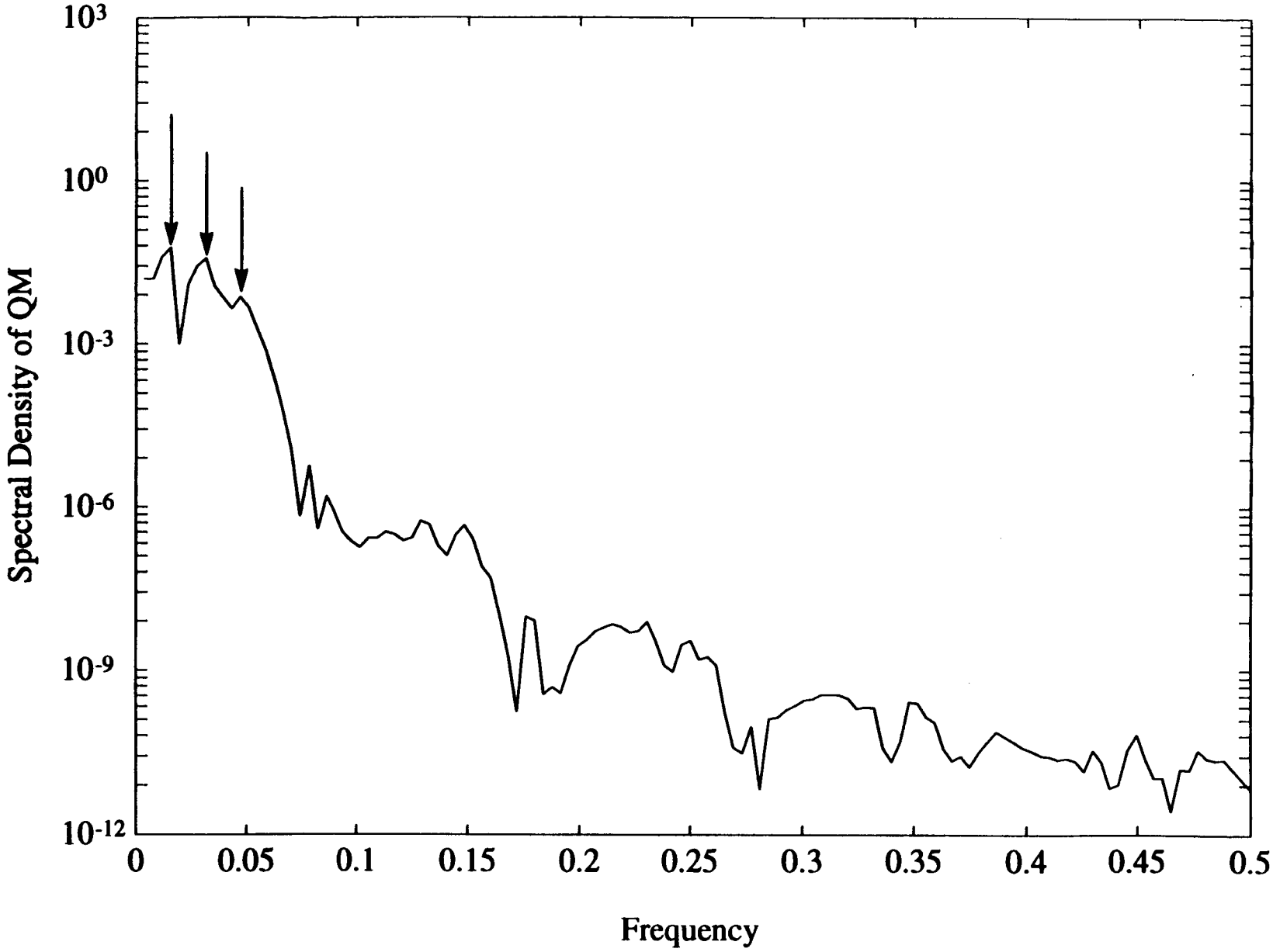

Figure 4-20. Power spectrum for case 200, based on Fast Fourier Transform of the $Q_M(t)$ time series

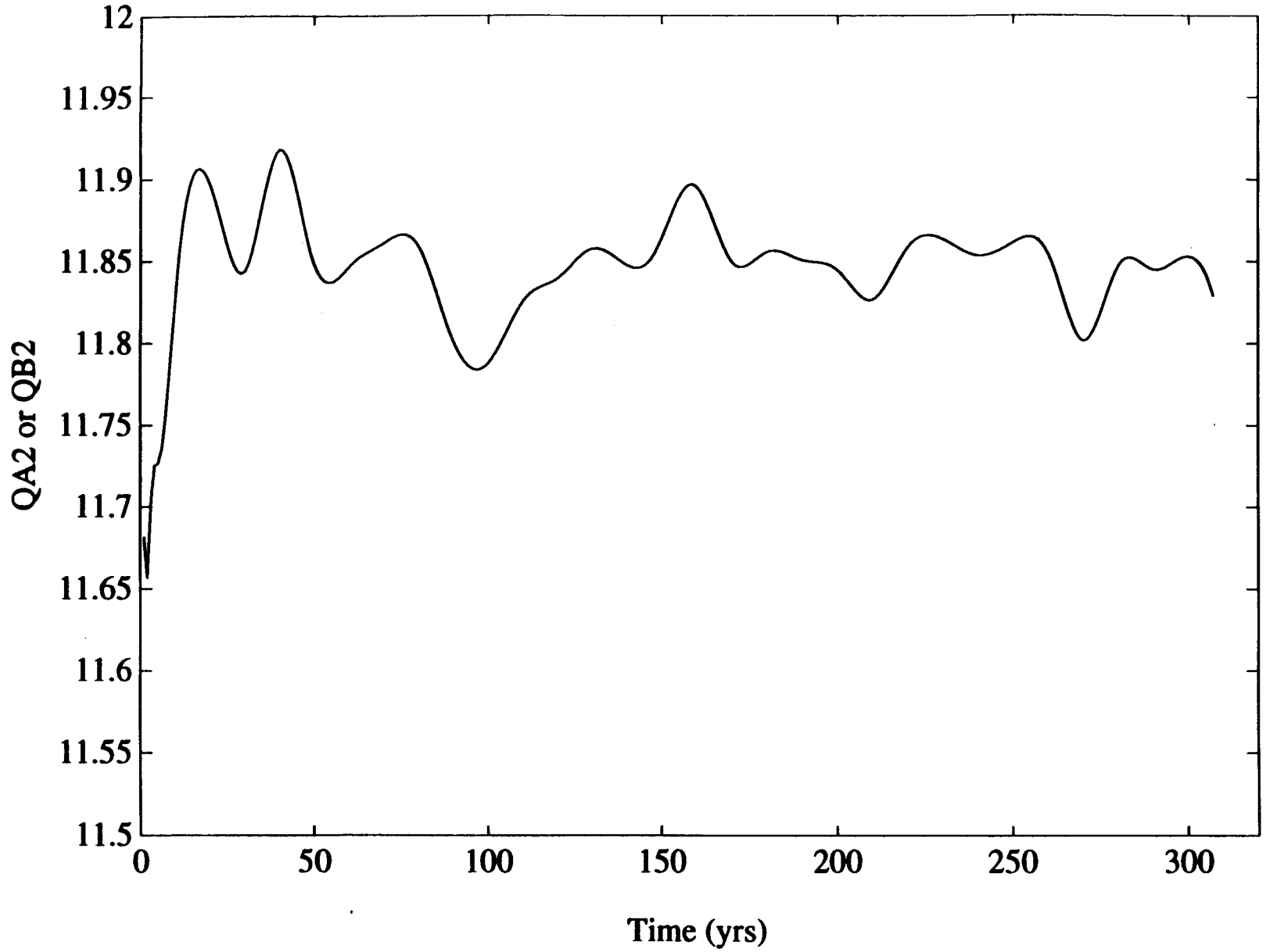

Figure 4-21. Temporal variation of lateral (North-South) outflows through boundaries for case 200. QA2 and QB2 represent outgoing discharge rates through South and North boundaries. They are identical.

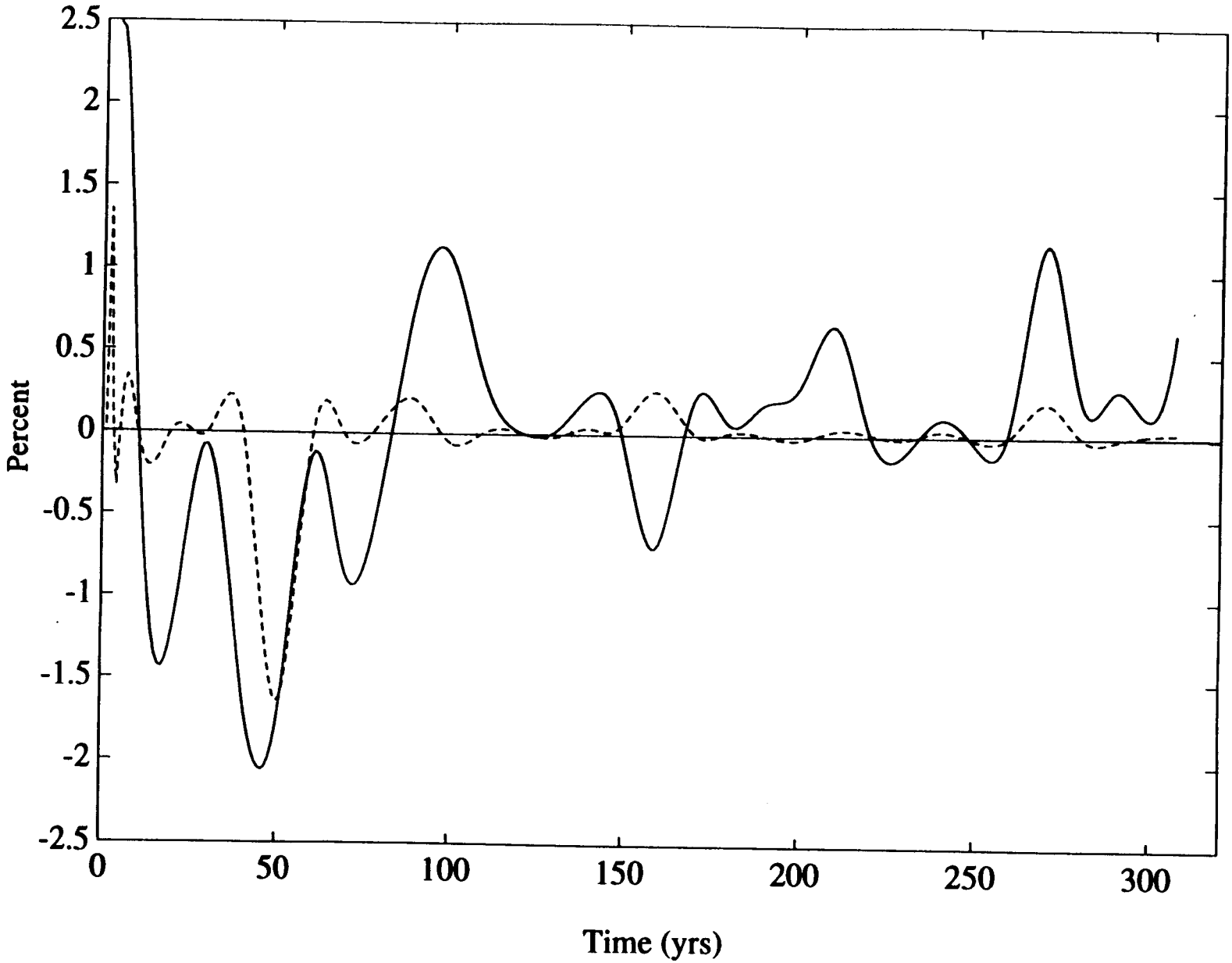

Figure 4-22. Relative measures of rate of change of mass (in percent) and numerical error as a function of time for case 200. Solid line: Measure of rate of change of total mass $\epsilon(t)$. Dashed line: Measure of mass balance error on discharge rates, $\eta(t)$.

instance, that the steady-state solution exists but is physically instable, resulting in oscillatory behavior.

Figure 4-23 further indicates that the North-South lateral flow may be essentially localized near the two regions where the fault intersects these boundaries. This figure displays a snapshot view of pressure contours in a horizontal cross-section (X-Y), at time t=10 years. The elongated feature at the center corresponds to the location of the fault. Note that the flow is strictly not two-dimensional, although it is constrained to be quadrant-symmetric. The existence of significant flow in the Y-direction may be due to the lack of realism of the pressure conditions imposed at the North-South boundaries, particularly where they are intersected by the fault. The resulting three-dimensional and oscillating flow pattern deserves further analysis, although some partial conclusions have already been drawn (see also conclusions in next chapter).

4.4 MISCELLANEOUS SENSITIVITY ANALYSES

Finally, this section concludes with a description of some additional tests performed for the purposes of sensitivity analysis. First, we present simulation results for a variant of case 100, with initial and boundary conditions extracted from the steady-state solution of case 2 (q_0=50 mm/year), and a surface flux q_o = 0 mm/year. In other words, using wet initial-boundary conditions, we introduce fault and dip, and simulate the hydrostatic case. The resulting solution, depicted in Figure 4-24, is clearly non-symmetric. Moreover, the effect of layering is visible, although slight.

Secondly, in order to test the consistency of results obtained from the various possible logical pathways for setting up consistent initial-boundary conditions (Figure 3-9), an additional set of simulations has been conducted. Results from case 2 have been input, as discussed previously, as initial and boundary conditions into case 20. Likewise, this simulation uses the "pseudo" steady-state results of case 20 as the starting point for getting to case 200. By comparing the results obtained through these two different logical pathways, identified as alternatives 1 and 2, the importance of initial-boundary conditions in such a flow system is assessed.

Figure 4-25 presents a contour plot of the difference in pressure head observed between these simulations. Note that the region plotted is only a part of the flow domain, for reasons of clarity. It is observed that, indeed, the two alternative simulations yield results different by as much as 6 percent of the maximum (in absolute value) pressure head found within the domain. Minimal differences are observed away from the fault zone, not surprisingly, since all the flow action occurs around the fault zone. Similar observations are made in Figure 4-26 depicting pressure head differences at five transects around the fault zone. Symmetry is not preserved due to the existence of the dipping angle. The upstream matrix-fault interface, at node 14, exhibits the maximum difference in pressure head.

It is not clear, at the moment, which one of the two "logical pathways" should be recommended. One may argue that a 6 percent difference is acceptable. Nevertheless, it may

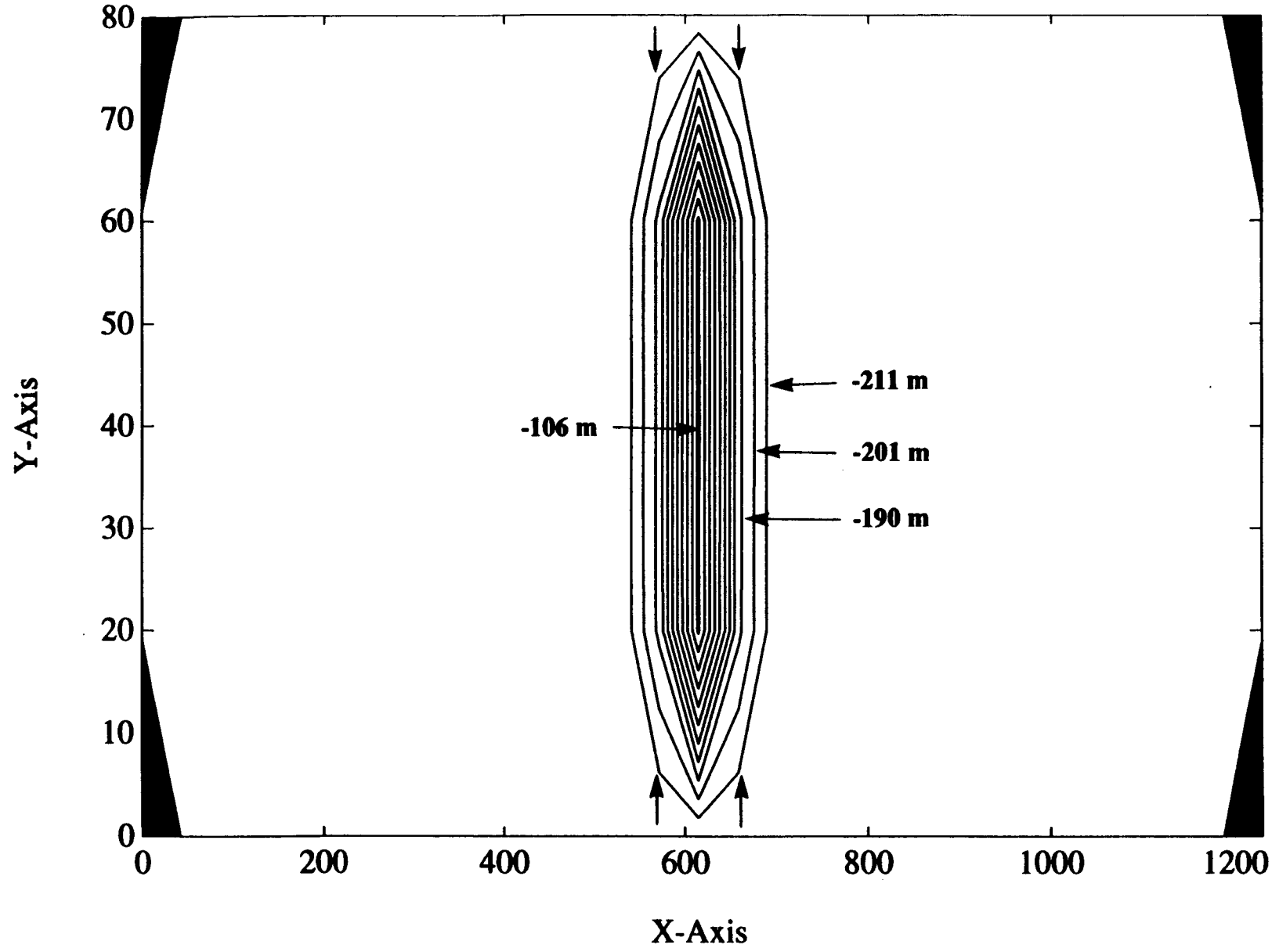

Figure 4-23. Pressure head contours in a horizontal cross-section at time t = 10 years for case 20

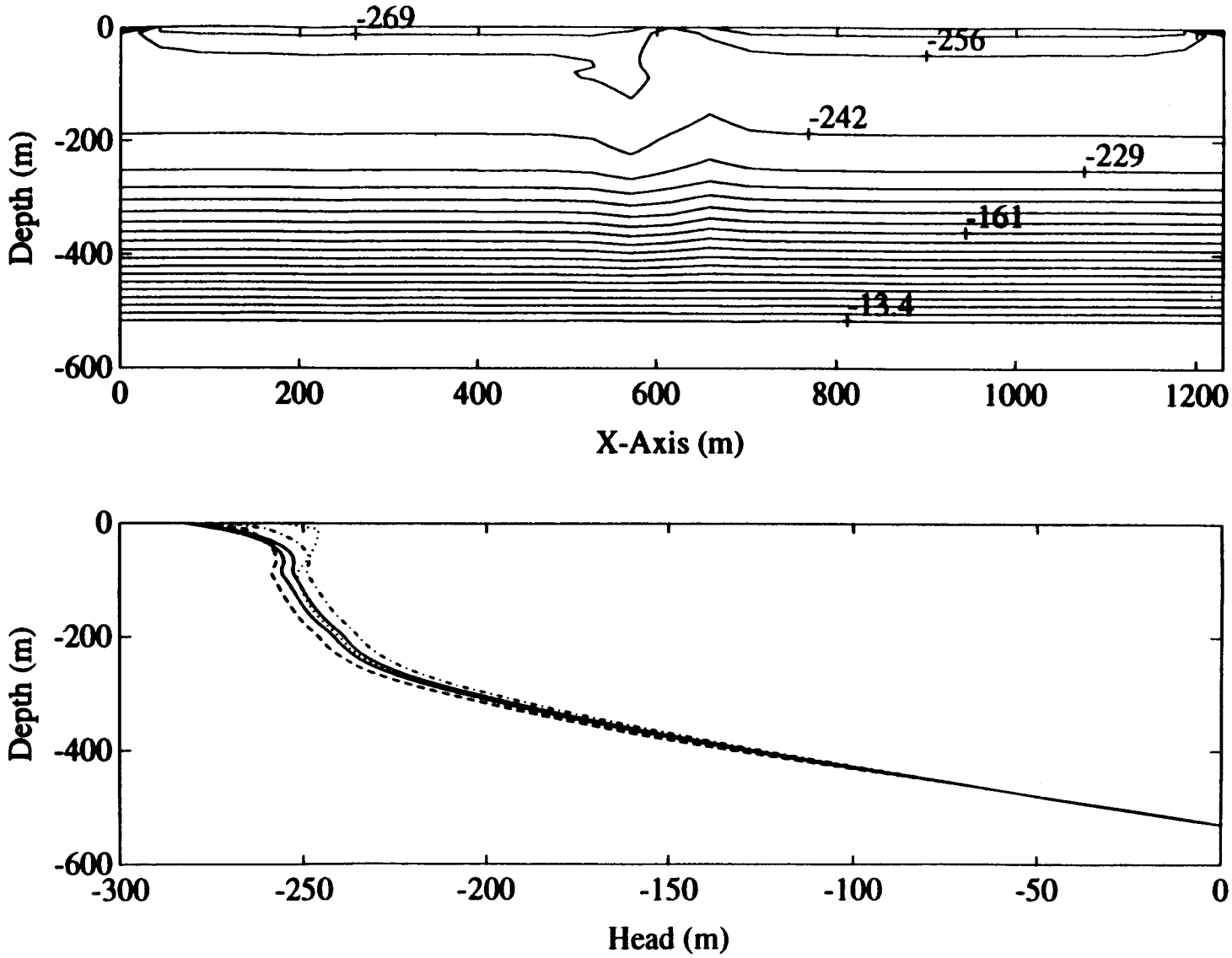

Figure 4-24. Pressure head results for t = 500 years. Case is a variation of case 100 (q_0 = 0 mm/year, with a fault) with initial-boundary conditions from case 2 (q_o = 50 mm/year, without a fault). Above: Contour plot at plane Y = 40 m. Below: Profile at different transects. The isovalues of pressure in the contour plot are given with increment Δh = 13.4m.

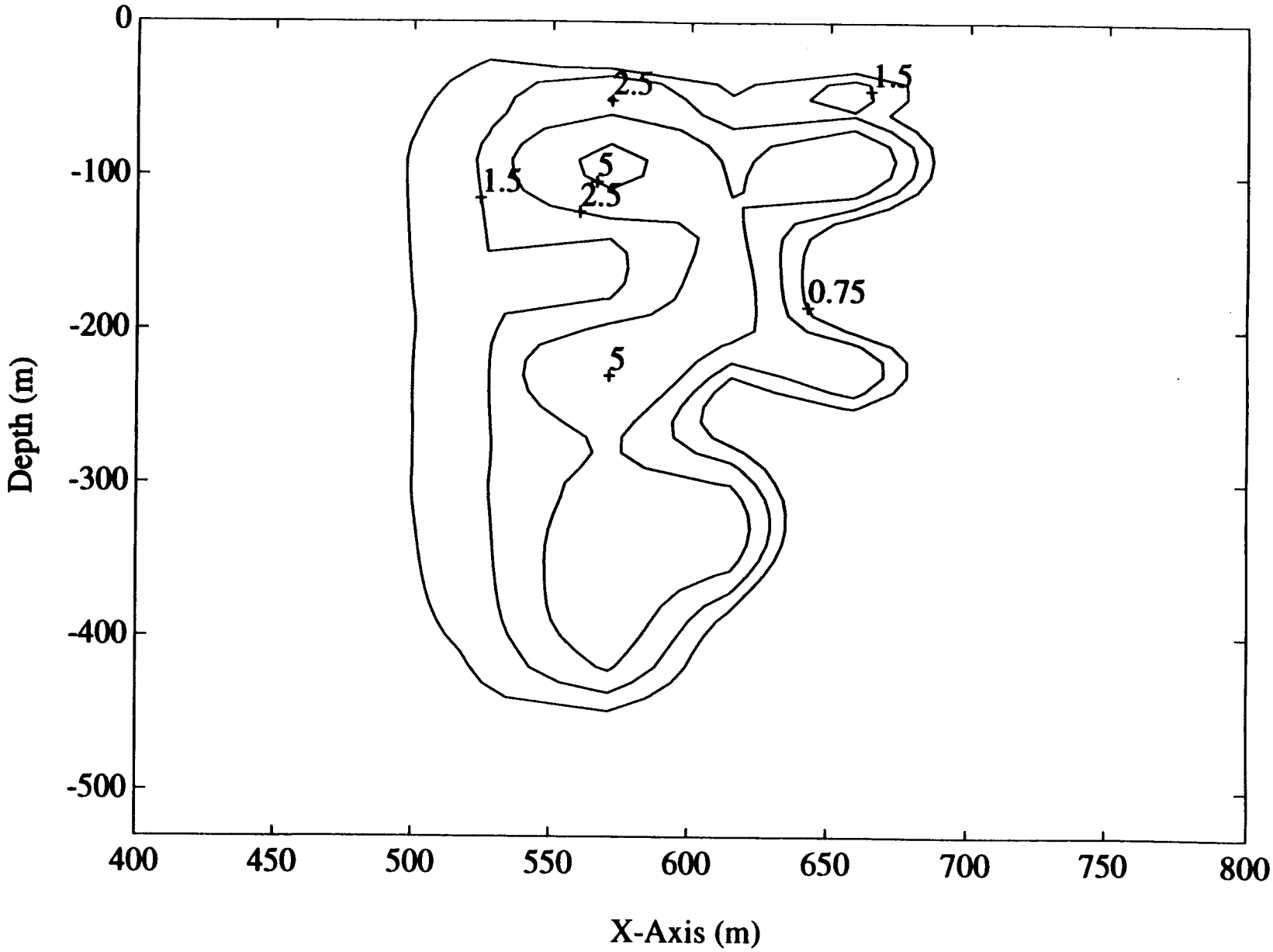

Figure 4-25. Contour plot of difference in pressure head at t = 120 years for alternatives 1 and 2

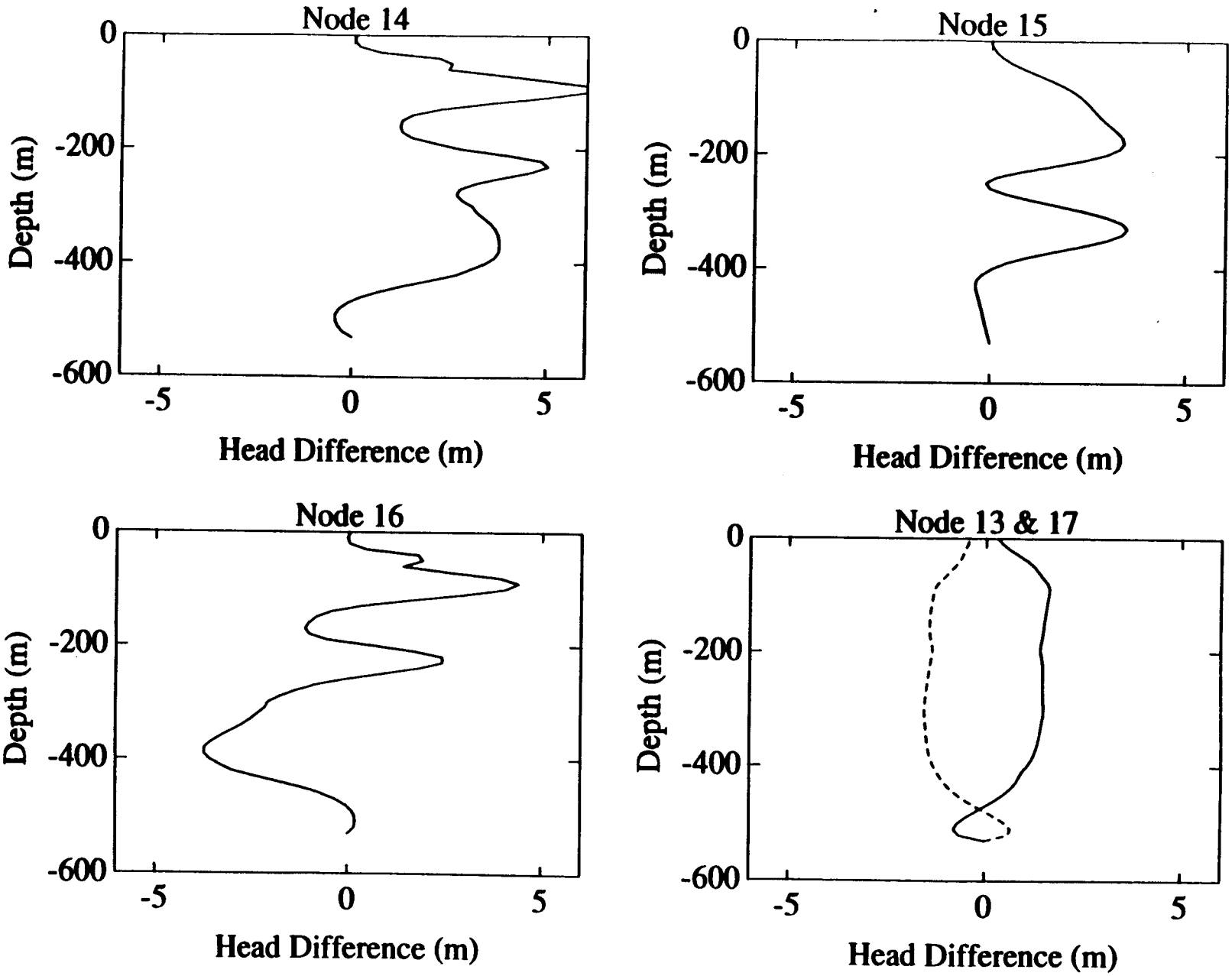

Figure 4-26. Pressure head difference at t = 120 years for alternatives 1 and 2 at five transects

be worth investigating systematically the conditions under which the difference may increase or decrease.

5 SUMMARY AND CONCLUSIONS

A hypothetical test problem was developed in order to study the effect of bedding on flow (represented by five layers), the presence of a subvertical fault zone (represented by a thin layer of very coarse material), and the effect of inclination of the beds (dipping six degrees eastward). A number of auxiliary tests were also conducted using variations on these hypothetical data. There are some similarities between this hypothetical problem and Yucca Mountain's stratigraphy, but since all site properties are not used, these simulations are not representative of the Yucca Mountain flow conditions.

First, it was observed that initial-boundary conditions consistent with other properties of the system are difficult to postulate from few measurements. In this study, a method was devised for generating initial-boundary conditions that are consistent to a steady-state flow with (i) the assumed input infiltration rate, and (ii) the assumed material properties of the modeled cross-section. For instance, artificial boundary conditions are needed for the East-West and for the North-South lateral boundaries. This is due in part to the fact that the cross-section is represented as a rectangular domain bounded by artificial (in contrast to natural) boundaries.

Recognizing that there may not be natural initial-boundary conditions that can be used for the more complex problems, a method of successive approximation was implemented. This method uses solutions of auxiliary flow problems to set-up pressure conditions for the more complex problems. Unfortunately, for the "thin slice" (Y-dimension small compared to X and Z dimensions) simulations reported in this study, the results suggest that it is particularly difficult to develop "consistent" initial-boundary conditions in the case where the fault intersects lateral boundaries (in the case at hand, the North-South oriented fault intersected the North-South boundaries). An oscillating flow regime was obtained at large times, i.e., after all initial transients died out, and this occurred both for a horizontal and dipping stratigraphy. After inspection, it was concluded that the oscillations were numerically significant, and indicated an intrinsic physical instability of the flow system. Also, most of the observed oscillations appeared to be due to fluctuating ingoing/outgoing lateral flow to and from the North-South, fixed pressure boundaries. This process appeared to be localized in regions where the fault intersects these boundaries, although this requires further confirmation.

Under the above-mentioned conditions, the variably saturated flow system is not only unsteady in an oscillatory fashion, but also three-dimensional, and this in spite of the "thin slice" geometry adopted in this study. To be sure, a strictly two-dimensional flow pattern could have been "forced" by imposing no-flux conditions at the North-South boundaries. This alternative may be overly constraining, but should be tried in future and compared to the "consistent" fixed pressure approach implemented in this study. It remains to be seen whether the resulting two-dimensional system would be physically stable in the presence of a highly contrasted fault zone and/or dip angle. The question of selecting artificial East-West boundary conditions would also remain open. For these, we would use the same "consistent" approach as before (pressure conditions obtained from auxiliary solutions). The choice of auxiliary solutions may be revised.

Furthermore, recognizing the ambiguous nature of regions where a fault intersects an artificial boundary, we advocate exploring further the issue by comparing thin slice or two-dimensional results to those obtained in a fully three-dimensional domain enclosing the fault in such a way that no lateral boundary is intersected by the fault. In addition, interpretations of results should be based on detailed flux distributions, not just pressure head distributions. The fluxes themselves could thereafter be used to compute groundwater velocities and travel times, and to delineate high velocity flowpaths. Given the results obtained here, the possibility of physical instability of the system will be worth keeping in mind.

Finally, we recognize the need for introducing in future work data that are more directly representative of the Yucca Mountain site. The stratigraphy should be refined regarding the spatial configuration of geologic units, the orientation of the fault, the existence of a fault offset of the beds due to fault slip, the replacement of the exponential conductivity curve with the smoother van Genuchten-Mualem curve, the increase in contrast of some of the fault properties, a more refined mesh to simulate a thinner fault zone, and generally a more careful selection of the unsaturated parameters of the fault and of the rock matrix in each geologic unit. In summary, based on the experience and knowledge gained during this part of the study, and with the use of a revised set of data, a more detailed processing of simulated flow that includes flux distributions, and alternative approaches to domain geometry and boundary conditions already outlined, it is expected that realistic and informative results can be obtained.

6 REFERENCES

Ababou, R. 1991a. *Approaches to Large Scale Unsaturated Flow in Heterogeneous, Stratified, and Fractured Geologic Media.* Report NUREG/CR-5743. Washington, D. C.: U. S. Nuclear Regulatory Commission (NRC).

Ababou, R. 1991b. Three-dimensional flow in heterogeneous geologic media: High-resolution simulation. Proceedings, International Hydrology and Water Resources Symposium. Perth, Australia: The Institution of Engineers, Australia. *Nat. Conf. Publ.* 92/22 3: 732-737.

Ababou, R. 1988. *Three-Dimensional Flow in Random Porous Media.* Ph.D thesis. Dept. of Civil Enginering, 2 vols. Cambridge, Massachusetts: Massachusetts Institute of Technology: 833.

Ahola, M., and B. Sagar. 1992. *Regional Groundwater Modeling of the Saturated Zone in the Vicinity of Yucca Mountain, Nevada. Iterative Performance Assessment - Phase II.* CNWRA92-001. San Antonio, Texas: Center for Nuclear Waste Regulatory Analyses.

Mattson, S. R., J. L. Younker, T. W. Bjerstedt, and J. R. Bergquist. 1992. Assessing Yucca Mountain's natural resources. *Geotimes.* January: 18-20.

Montazer, P., and W. E. Wilson. 1984. Conceptual hydrologic model of flow in the unsaturated zone, Yucca Mountain, Nevada. *U. S. Geological Survey Water Resources Investigations report 84-4345.* Denver, Colorado: 55.

Rockhold, M. L., B. Sagar, and M. P. Connelly. 1990. Multi-dimensional modeling of unsaturated flow in the vicinity of exploratory shafts and fault zones at Yucca Mountain, Nevada. *Proceedings of the First International Meeting on High Level Radioactive Waste Management.* La Grange Park, Illinois: American Nuclear Society 2: 1192-1199.

Rockhold, M. L., B. Sagar, and M. P. Connelly. 1989. *Three-dimensional Modeling of Unsaturated Flow in the Vicinity of Exploratory Shaft Facilities at Yucca Mountain, Nevada.* Richland, Washington: Pacific Northwest Laboratory.

Sagar, B., and A. K. Runchal. 1990. *PORFLO-3: A Mathematical Model for Fluid Flow, Heat and Mass Transport in Variably Saturated Geologic Media - Theory and Numerical Methods, Version 1.0.* WHC-EP-0042. Richland, Washington: Westinghouse Hanford Company.

Scott, R. B., and J. Bonk. 1984. *Preliminary Geologic Map of Yucca Mountain with Geologic Sections, Nye County, Nevada.* U. S. Geological Survey Open-File Report 84-494, scale 1:12,000.

Tompson, A. F. B., and L. W. Gelhar. 1990. Numerical simulation of solute transport in three-dimensional, randomly heterogeneous porous media. *Water Resour. Res.* 26(10): 2541-2562.

Townley, L. R., J. V. Turner, M. G. Trefry, and A. D. Barr. 1991. Groundwater flow patterns near lakes and wetlands: Modelling and field validation. Procedings, International Hydrology and Water Resources Symposium. Perth, Australia: The Institution of Engineers, Australia. *Nat. Conf. Pub.* 91/22 3: 732-737.

Townley, L. R., and M. G. Trefry. 1990. Two- and three-dimensional modelling of groundwater flow through the Koongarra uranium orebody. *Alligators Rivers Analogue Project.* P. Duerden ed. Australian Nuclear Science and Technology Organisation. Progress Report (1 June 1990 - 31 August 1990): 97-113.

U. S. Department of Energy. 1988. *Site Characterization Plan.* Yucca Mountain Site, Nevada Research and Development Area, Nevada, Volume II, Chapter 3.

APPENDIX A

CONSISTENT INITIAL AND BOUNDARY CONDITIONS: AN EXPLANATION

In this appendix, we elaborate on the term "consistent" initial and boundary conditions, and motivate the use of successive approximation for generating initial-boundary conditions. One way to generate artificial lateral boundary conditions may be to impose a pressure profile inferred from in-situ measurements of moisture, suction or other indirectly related observations, as done in Chapter 3 of this report. There is, however, one difficulty with that approach, which motivated a change of strategy in the choice of initial-boundary conditions in the rest of the report. To explain the difficulty with the above-mentioned approach, we will analyze a very simplified case for illustration.

Consider the case where the actual in-situ moisture profile is hydrostatic, and assume that the investigator is indeed correct in assuming $q_o = 0$, and $h_T(Z) = Z$ for the net infiltration rate. Assume further that a measured moisture profile is available. We call this the "true" moisture profile $\theta_T(h)$, as depicted in Figure A-1a. However, because there is a great uncertainty in the water retention curve, the investigator only knows an approximate or "false" curve: $\theta_F(h)$, as shown in Figure A-1a. The solution of a steady simulation with this "false" water retention curve will give the "false" moisture profile: $\theta_F(Z)$

Upon linearizing the retention curves as shown in Figure A-1b (and this only for the purposes of quantifying the resulting errors), the "investigator" would obtain successively the following results. First, inverting moisture curves to obtain suction yields:

$$h_F(Z) = \theta_F^{-1}\left[\theta_T(Z)\right] \quad . \tag{A-1}$$

Linearization of the water retention curves (only for clarity of expose) yields:

$$\begin{aligned} \theta_F(h) &\approx C_F \cdot h \\ \theta_T(h) &\approx C_T \cdot h \quad . \end{aligned} \tag{A-2}$$

The final result obtained by the "investigator" is therefore:

$$h_F(Z) = \frac{C_T}{C_F} \cdot Z \quad . \tag{A-3}$$

This result should be compared to the true hydrostatic profile,

$$h_T(Z) = Z \quad . \tag{A-4}$$

Obviously, an error has resulted from this procedure. In the case at hand, we have $C_T > C_F$ in Figure A-1, and it follows from the above relations that the "false" suction profile is dryer than the "true" hydrostatic profile. Moreover, this error will propagate into the estimation of vertical flux as calculated by Darcy's law,

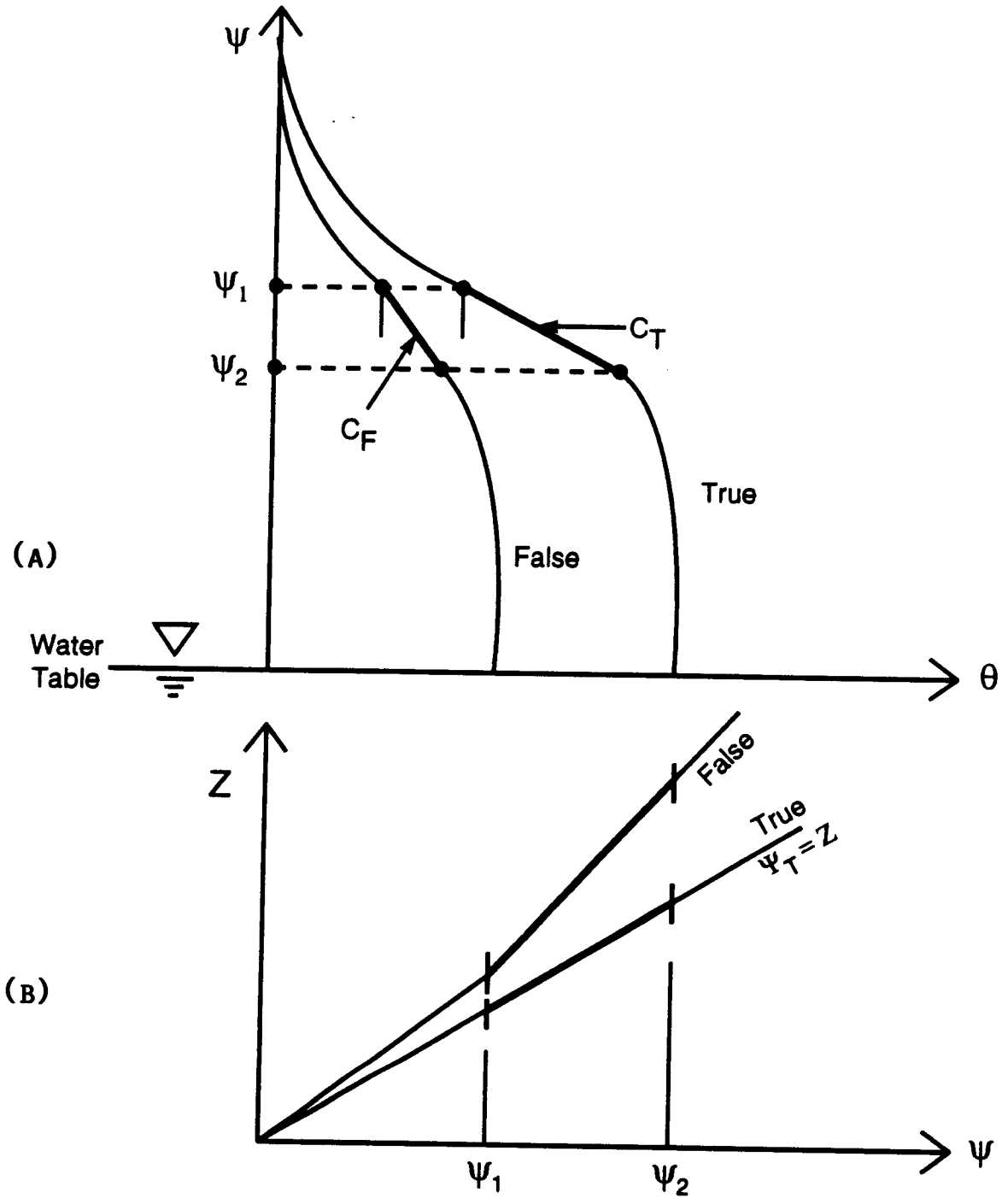

Figure A-1. Schematic representation of the effect of uncertainty in the water retention curve. (a) "true" and "false" retention curves. (b) Linearized "false" pressure head profile.

$$q = + K(h)\left(\frac{\partial h}{\partial z} - 1\right) \quad . \tag{A-5}$$

That is, a non-zero flux may be obtained as a result of the above procedure, while the true solution is hydrostatic (zero flux). Furthermore, similar inconsistencies will also occur in the following, more realistic case of a non-hydrostatic system:

$$q_0^{\text{Assumed}} = q_0^{\text{True}} \neq 0 \quad . \tag{A-6}$$

Here, errors will be introduced in due to the "false" curve K(h) being used in simulation. Finally, the situation would be even worse if

$$q_o^{\text{Assumed}} \neq q_0^{\text{True}} \quad . \tag{A-7}$$

Note that the proposed approach of successive approximation avoids using the "observed" profile h(Z) as initial-boundary condition, and therefore, none of the above problems will occur.